ACS Catalysis

pubs.acs.org/acscatalysis Research Article

Highly Durable C_2 Hydrocarbon Production via the Oxidative Coupling of Methane Using a $BaFe_{0.9}Zr_{0.1}O_{3-\delta}$ Mixed Ionic and Electronic Conducting Membrane and La_2O_3 Catalyst

Georgios Dimitrakopoulos,* Bonjae Koo, Bilge Yildiz, and Ahmed F. Ghoniem*

Cite This: *ACS Catal.* 2021, 11, 3638−3661 Read Online

ACCESS | Metrics & More | Article Recommendations | Supporting Information

ABSTRACT: The oxidative coupling of methane (OCM) is an attractive technology for the production of ethane (C_2H_6) and ethylene (C_2H_4); and significant performance and efficiency gains as well as reduced carbon dioxide (CO_2) emissions are expected when OCM takes place within mixed ionic and electronic conducting (MIEC) ceramic membrane reactors (CMRs). So far, research on OCM in CMRs has been limited to unstable and incompatible materials investigated under short-term measurements that hinder upscaling and commercial application. To this end, this work demonstrates long-term stable OCM performance enabled by a $BaFe_{0.9}Zr_{0.1}O_{3-\delta}$ (BFZ91) perovskite utilized as the oxygen-ion MIEC membrane and lanthanum oxide (La_2O_3) used as the OCM catalyst. Experimental measurements conducted in the temperature (T) range of 750−900 °C and at inlet methane (CH_4) mole fractions ($X^{in}_{CH_4}$) of 0−30% revealed a highly stable performance during 23 days of continuous operation, which was further confirmed by material characterization. Under the aforementioned operating conditions, BFZ91 offers a high oxygen (O_2) permeation flux (J_{O_2}) between 0.5−1.5 (μmol/cm^2/s); CH_4 conversion (C_{CH4}) reached ∼35% while the selectivities to C_2H_6 ($S_{C_2H_6}$) and C_2H_4 ($S_{C_2H_4}$) were as high as ∼50% and ∼40%, respectively, showing a strong dependency on the operating conditions. Yields of C_2H_6 ($Y_{C_2H_6}$) and C_2H_4 ($Y_{C_2H_4}$) in the range of 1−5% and 1−7%, respectively, were measured, with more C_2H_4 being produced at higher T. In the absence of La_2O_3, C_{CH_4} and C_2 (C_2H_6 and C_2H_4) yields are lower confirming that BFZ91 does not promote CH_4 oxidation, reforming, or coupling on its surface at high rates. The OCM performance of BFZ91 with La_2O_3 was also found to be stable under partial O_2 consumption and pure CH_4 conditions. Furthermore, a detailed analysis of the mixture composition allowed the identification of the primary reactions in the OCM chemistry. Our results reveal that within our reactor, CH_4 full oxidation to CO_2 and steam (H_2O) happens simultaneously with CH_4 oxidation to C_2H_6 and H_2O (both on the La_2O_3 catalyst), but the production of the valuable C_2H_4 is primarily taking place through the C_2H_6 non-oxidative dehydrogenation in the gas phase; this reaction was not found to proceed on the La_2O_3 catalyst. Besides the promise of the investigated materials toward commercialization, the methods to study the OCM chemistry and the membrane catalyst coupling presented here are expected to promote further advances in the field of OCM.

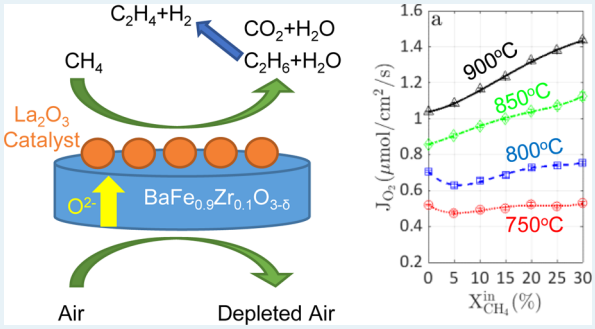

KEYWORDS: *oxidative coupling of methane, ceramic membrane reactors, $BaFe_{0.9}Zr_{0.1}O_{3-\delta}$ mixed ionic−electronic conductor, La_2O_3 catalyst, OCM chemistry, long-term OCM measurements*

1. INTRODUCTION

C_2H_4 is one of the most important commodity chemicals worldwide with a 2018 global production of ∼185 million metric tons (MMT).[1] During 2019, the production of C_2H_4 in the United States (US) was the highest among other chemicals and plastics reaching ∼32 MMT.[2] Its high demand is related primarily to its use as a building block in the production of polymers, such as polyethylene and polyvinyl chloride.[3] Other uses of C_2H_4 include the synthesis of intermediate chemical compounds and its utilization as a plant hormone in agriculture.[3] Given its high demand, projections reveal that the global C_2H_4 production could rise to ∼260 MMT by 2023[4] and in the long term to ∼290 MMT by 2030.[1] The price of C_2H_4 is relatively high and can exhibit significant fluctuations during a calendar year. For example, the C_2H_4 contract price in the US during 2019 ranged between $530−650 per metric ton driven by

Received: November 9, 2020
Revised: February 18, 2021

https://dx.doi.org/10.1021/acscatal.0c04888
ACS Catal. 2021, 11, 3638−3661

monthly changes in the C_2H_4 demand and production and by variations in the feedstock price.[5]

C_2H_4 is primarily produced by steam cracking of naphtha or ethane[3,6] but other feedstocks such as propane, butane, and gas oil are also used.[7] Naphtha is the main feedstock in Europe and Asia while ethane crackers are mostly used in North America and the Middle East.[8] Steam-cracking reactions are highly endothermic and take place at temperatures between 750−950 °C.[7] From an energy consumption and yield point of view, when using C_2H_6 as the feedstock, the process requires ∼12.5−21 GJ per ton of produced C_2H_4[9] and C_2H_4 yields are as high as ∼80%.[7,9] For naphtha, the process becomes more energy intensive and requires ∼14−22 GJ per ton of produced C_2H_4,[9] while the C_2H_4 yields drop significantly to ∼30% because of the formation of various byproducts such as methane, propylene, butane, and other fuel oils.[7,9] For naphtha, one also has to account for variations in its composition which affect the final product yield.[7] Besides the high energy requirements and the corresponding CO_2 emissions, cracking reactions are thermodynamically limited because of species accumulation in the reactor (e.g., H_2 formation from C_2H_6 pyrolysis). Moreover, C_2H_6 and naphtha crackers suffer from severe carbon deposition, a safety hazard that requires periodic shutdown.[6] Finally, the purification of C_2H_4 is another challenge with a significant energy penalty given that it is based on high-pressure cryogenic distillation taking place at temperatures of −160 °C.[10]

An alternative to the production of C_2H_4 is the oxidative coupling of methane (OCM). The process was first suggested by Keller and Bhasin,[11] and it involves co-feeding CH_4 and O_2 in a single stream, which react in the presence of a catalyst at T = 650−900 °C to produce C_2 as follows:

$$2CH_4 + \frac{1}{2}O_2 \rightleftharpoons C_2H_6 + H_2O$$
$$\Delta H^{\circ}_{298K} \approx -176.9\ \text{kJ/mol}\ C_2H_6 \quad (1)$$

$$2CH_4 + O_2 \rightleftharpoons C_2H_4 + 2H_2O$$
$$\Delta H^{\circ}_{298K} \approx -281.8\ \text{kJ/mol}\ C_2H_4 \quad (2)$$

OCM has several advantages when compared to steam cracking including:[12] (1) reduced energy consumption because of the reaction exothermicity resulting in fewer CO_2 emissions; (2) the feedstock is natural gas (composed primarily of CH_4), which is currently cheap ($2.3−3/GJ) and widely produced in the US from shale reserves with future production increase from gas hydrate exploitation; (3) lower cost, due to the direct conversion of CH_4 to C_2 without the need for intermediate steps that require the use of syngas; and (4) formation of H_2O in the products because of the CH_4 reaction with O_2 removes equilibrium limitations and reduces downstream separation costs. However, OCM has four important challenges: (1) the process is kinetically controlled because at equilibrium, CH_4 partial or full oxidation takes place;[13] (2) the produced C_2 species can pyrolyze at the OCM operating T and this creates the need to reduce the T and the residence time at the expense of catalyst performance and CH_4 conversion, respectively; (3) the process requires a selective and long-term stable catalyst to drive the reaction at relatively low T; and (4) CH_4 oxidation forms byproducts, such as carbon monoxide (CO), CO_2, and so forth, that reduce the C_2 selectivity and yield.

Co-feeding CH_4 and O_2 in a single-stream reactor relies on a fixed-bed catalyst to drive OCM. However, this conventional OCM technology has three major limitations: (1) it needs pure O_2, whose production is based on cryogenic air separation, and hence, creates a significant energy penalty;[14] (2) while the OCM stoichiometric CH_4/O_2 ratio for C_2H_4 production is 2 (reaction 2), in practice, ratios of 5−10 are required to avoid deep oxidation of CH_4, and hence, most of it remains unconverted or forms undesired species; and (3) the reaction exothermicity (reactions 1 and 2) combined with nonuniform conversion along the catalyst bed results to large T gradients, which is a safety risk and could lead to local catalyst deactivation along the reactor, thus reducing the C_2 yields further.

Despite intense research to design selective OCM catalysts,[12,15] only one commercial reactor has been reported to date but its C_2 yield is currently unknown.[16] Early techno-economic analyses proposed that economic viability of the conventional OCM process requires a single-pass C_2H_4 yield higher than 25%.[12,17,18] However, more recent investigations focusing on C_2H_4 production in Europe propose that the fuel-to-chemicals efficiency of naphtha crackers can be achieved from conventional OCM only if single-pass C_2H_4 yields around 45−50% can be obtained.[19,20] Similar studies show that besides efficiency, the C_2H_4 price from plants employing the conventional OCM technology can compete with naphtha crackers only if OCM yields higher than 30% can be achieved.[21] This is because of the large capital cost of units required to separate C_2 from the gaseous stream,[10,21] and the recombination of syngas (produced from secondary reactions) back to CH_4. Operating expenses related to the cost of natural gas and electricity significantly affect the C_2H_4 production price.[21] To decrease the cost of the separation units, and hence, the C_2H_4 price, it has been suggested that the target yields should be achieved with high C_2 selectivity catalysts compared to high CH_4 conversion catalysts.[21]

An alternative technology for OCM that has the potential to improve upon the conventional OCM relies on oxygen-ion conducting ceramic membrane reactors (CMRs). A recent techno-economic analysis suggested that the price of C_2H_4 produced from membrane-based OCM plants could potentially compete with naphtha crackers if C_2H_4 yields higher than 30% can be achieved.[22] Note, however, that estimating the price of a membrane reactor has its own challenges given that the large-scale deployment of these reactors has so far been limited. The same study also confirms that significant CO_2 emission reduction can be attained with CMRs.[22] OCM in CMRs enables process intensification given that pure O_2 can be separated from an O_2 containing gaseous stream and be converted to added-value chemicals in the same reactor, hence reducing the reactor size and cost. In addition, given that increased CH_4/O_2 ratios generally allow for higher C_2 selectivity,[13] it has been demonstrated that CMRs offer higher C_2 selectivity compared to the conventional OCM.[23−25] Moreover, the gradual introduction of O_2 through the membrane allows for a better thermal management with decreased T gradients. Finally, OCM in CMRs takes place along the entire reactor length in contrast to conventional fixed-bed OCM reactors, where the C_2 production is confined at the initial stages of the catalyst followed by the pyrolysis of the desired species or by secondary undesired reactions that reduce the C_2 yield.[26] It is evident that in OCM with CMRs, the design of the reactor (its geometry, in particular) is another important variable that needs to be explored and optimized.

CMRs consist of two different gaseous streams separated by a ceramic oxide material.[12,14,27] Membrane materials commonly used in oxygen-ion CMRs exhibit mixed ionic and electronic

https://dx.doi.org/10.1021/acscatal.0c04888
ACS Catal. 2021, 11, 3638−3661

conductivity and hence allow the transport of O_2 (in the form of ions) from a high O_2 chemical potential (μ_{O_2}) stream to a low μ_{O_2} stream without external polarization, that is, it is a purely thermochemical process driven by surface reactions on the gas−membrane interfaces coupled with the diffusion of charged species (oxygen vacancies, small polarons etc.) within the material. When air is introduced on one stream (the air side) and CH_4 on the other (the CH_4 side), O_2 is converted to oxygen ions (O^{2-}) on the air side surface, which are then incorporated into the material. O^{2-} diffuse through the membrane to the CH_4 side via an oxygen vacancy-mediated mechanism that also involves the transport of electrons and electron holes to preserve charge neutrality in the bulk of the material.[28−31] At the CH_4 side surface, CH_4 may react either with O^{2-} directly on the surface or with desorbed O_2 in the gas phase. In the presence of a catalyst, O_2 and CH_4 react on its surface to form C_2 species and other products.

The success of OCM in CMRs requires a membrane-catalyst configuration that can operate with acceptable J_{O_2} and high C_2 yields under long times without the formation of undesired phases that could degrade the performance. The former, that is, the value of J_{O_2}, is a challenge in CMRs because J_{O_2} can only be controlled indirectly by the operating conditions and the membrane properties. These establish a μ_{O_2} gradient along the two membrane sides and do not allow for the direct control of O_2 through the membrane. The latter, that is, undesired phases, can arise because of: (1) decomposition of the material on the OCM side due to operation under a low partial pressure of O_2 (P_{O_2}); (2) cation segregation from the bulk to the surface induced by elastic and electrostatic interactions;[32] (3) reaction of the materials with gaseous species (e.g., formation of stable surface carbonate species because of CO_2 in the gaseous stream); and (4) reaction of the membrane with the OCM catalyst forming undesired phases.[33]

Prior work on OCM using oxygen-ion conducting CMRs has focused on the development of membrane-catalyst materials with high J_{O_2} and increased C_2 selectivity and yield.[34,35] Unfortunately, the trend in OCM is that high C_2 selectivity is accompanied by low CH_4 conversion and vice versa, and this limits the maximum C_2 yield that can be obtained. For example, Igenegbai et al. investigated OCM using dense $BaCe_{0.8}Gd_{0.2}O_{3-\delta}$ (BCG) and nickel-doped $La_{0.8}Sr_{0.2}Ga_{0.8}Mg_{0.2}O_{3-\delta}$ (LSGM) disk-shaped membranes employing BCG and LSGM porous supports, respectively, acting as OCM catalysts.[36] Stable operation with C_{2+} (C_2H_6, C_2H_4 and higher hydrocarbons) selectivity of ∼80% was achieved at T = 810 °C with the former, while degradation was observed for the latter because of carbon deposition.[36] Despite the high selectivity, a C_{2+} yield of ∼1−2% was obtained because of low CH_4 conversion.[36] Garcia-Fayos et al. used $Ba_{0.5}Sr_{0.5}Co_{0.8}Fe_{0.2}O_{3-\delta}$ (BSCF) membranes and screened several catalysts.[37] C_{2+} yields of ∼15% were obtained at 900 °C when using a tubular membrane packed with a 2 wt % Mn_xO_y, 5 wt % Na_2WO_4 catalyst supported on SiO_2; C_{2+} yields were lower when a disk-shaped membrane configuration was employed.[37] Othman et al. investigated the performance of $Bi_{1.5}Y_{0.3}Sm_{0.2}O_{3-\delta}$ (BYS) catalysts deposited on $La_{0.6}Sr_{0.4}Co_{0.2}Fe_{0.8}O_{3-\delta}$ (LSCF) hollow fiber membranes;[38] they found that an in situ preparation-deposition of the catalyst on the membrane is superior when compared to the traditional wash-coat deposition method. C_{2+} selectivity and yield of 79 and 39%, respectively, were obtained at 900 °C. Tan et al. also used LSCF hollow fiber membranes with the $SrTi_{0.9}Li_{0.1}O_{3-\delta}$ catalyst;[39] at 975 °C, they obtained a maximum C_2 yield of ∼21%. Akin and Lin investigated OCM within tubular BYS membranes;[25] at 900 °C, C_2 selectivity and yield of 54 and 35% were obtained, respectively. In a similar work using disk-shaped BYS membranes, Zeng and Lin showed that the C_2 selectivity and yield at 900 °C were 35 and 8%, respectively, thus highlighting once more the influence of the membrane geometry and the membrane-catalyst choice on the C_2 yield.[40]

Although some of the aforementioned membrane-catalyst systems can deliver C_2 yields higher than early and recent target values,[17−19,21,22] their long-term stability is a major concern. For example, BSCF membranes are known to decompose under reducing conditions[41] and to form barium carbonates at high T even with traces of CO_2 from air under long-term operation;[42] on the OCM side, the degradation is more intense because of increased CO_2 concentrations.[43] In addition, the reaction of barium in BSCF with the SiO_2 support of the Mn_xO_y−Na_2WO_4 catalyst is thermodynamically favorable under OCM conditions. This reaction forms insulating barium−silicon oxide layers on the OCM side, hence reducing J_{O_2} and the C_2 yield.[37,44] LSCF is also unstable and prone to decomposition in a reactive environment,[45,46] while the reaction with SiO_2 is unavoidable.[47,48] For LSCF, strontium oxide and cobalt oxide surface segregation have been reported in the literature and are expected to reduce the performance under long-term operation.[49] Moreover, the transition of the SiO_2 catalyst support from the α-cristobalite phase to the amorphous phase observed at T ≥ 750 °C reduces the C_2 selectivity and confirms a clear correlation between OCM activity and catalyst support.[50,51] BCG was also found to partially decompose under OCM conditions, but this effect was not shown to decrease the C_{2+} yields as a function of time when CH_4 and air were co-fed in a single chamber reactor.[33] The addition of zirconium (Zr) in the B-site gave similar OCM performance compared to BCG and improved the resistance to decomposition;[33] however, the decomposition was not eliminated completely showing that under long term, the material does not survive the OCM conditions. Volatile elements should also be avoided as they impact the long-term stability. For example, bismuth oxide (Bi_2O_3) has a melting point equal to 817 °C; operation above this temperature results in the loss of bismuth because of evaporation.[52,53] Evaporation has also been observed for lithium at 800 °C.[54−56] These membrane-catalyst instabilities clearly demonstrate that research on OCM in CMRs should focus both on material performance and stability, which should be demonstrated under the long-term operation.

To meet the aforementioned performance and long-term stability criteria, the present work investigates OCM using a BFZ91 ceramic membrane coupled with La_2O_3 powder. BFZ91 has been shown to deliver a high J_{O_2} and to be stable structurally and in the presence of different hydrocarbon environments,[57,58] while La_2O_3 is one of the most active and stable OCM catalysts among the various doped and undoped rare earth oxides.[59−62] Both BFZ91 and La_2O_3 were characterized prior to the OCM measurements, and trends related to their properties are investigated and discussed. In the absence of La_2O_3, the BFZ91 membrane is relatively inactive toward the catalytic CH_4 decomposition or oxidation, and hence, it serves as a means to separate O_2 from air without converting much CH_4 to the (un)desired products. In the presence of La_2O_3, long-term

https://dx.doi.org/10.1021/acscatal.0c04888
ACS Catal. 2021, 11, 3638−3661

measurements conducted in a button-cell reactor demonstrate that the BFZ91-La_2O_3 combination is highly stable for 23 days in the stream, during which the temperature and inlet CH_4 mole fraction were varied between T = 750−900 °C and $X^{in}_{CH_4} = 0 - 30\%$, respectively. This is further confirmed by post-mortem material characterization showing the absence of secondary phases. To the best of our knowledge, this is the first time that materials with such a prolonged OCM lifetime are reported for the CMR technology. J_{O_2}, C_{CH_4}, C_2H_6 and C_2H_4 selectivity, yield, and activity (i.e., molar production rate scaled to the catalyst mass) ($\tilde{n}$) are used as performance metrics. Our results confirm that J_{O_2} is limited by both bulk diffusion and surface reactions at T = 750−800 °C; higher fluxes are obtained at T = 850−900 °C, during which surface reactions at the CH_4 side are accelerated. The maximum Y_{C_2} is ∼10% and it is obtained at T = 850 °C and $X^{in}_{CH_4} = 5\%$ during which $J_{O_2} \approx 0.91$ (μmol/cm^2/s) and $S_{C_2} \sim 39\%$. Experiments under partial O_2 consumption and pure CH_4 conditions also demonstrated a stable performance. For the latter, secondary phases were detected on the CH_4 side because of the highly reducing conditions under pure CH_4; however, our 3-day measurement showed no loss of performance as a function of time. Finally, the analysis of the gas-phase mixture composition near the CH_4 side of the membrane but within the La_2O_3 bed and comparison with outlet values allows to determine the primary reactions involved in the OCM chemistry. CH_4 full oxidation to CO_2 and H_2O, CH_4 oxidative coupling to C_2H_6 and H_2O and C_2H_6 non-oxidative dehydrogenation to C_2H_4 and H_2 are identified as the key OCM reactions within our reactor. We show that the first two reactions happen on the La_2O_3 catalyst, while the third is only taking place in the gas phase. This finding is important because it demonstrates that La_2O_3 facilitates the formation of C_2H_6 but the production of C_2H_4 within our reactor happens primarily in the gas phase through the non-oxidative dehydrogenation of C_2H_6 (NODHE).

2. EXPERIMENTAL SECTION

2.1. Material Synthesis. The BFZ91 powder was synthesized using a combined citric acid (CA)—ethylenediaminetetraacetic acid (EDTA) method. To form the perovskite oxide, stoichiometric amounts of $Ba(NO_3)_2$ (99.999%—Alfa Aesar), $Fe(NO_3)_3{\cdot}9H_2O$ (≥99.95%—MilliporeSigma) and $ZrO(NO_3)_2{\cdot}xH_2O$ (99.99%—MilliporeSigma) were first dissolved in purified water and subsequently mixed with CA (≥99.5%—MilliporeSigma) and EDTA (99.995%—MilliporeSigma) in a ratio of total metal cations:CA:EDTA = 1:1.5:1. The value of x in $ZrO(NO_3)_2{\cdot}xH_2O$ was estimated to be x = 2.1 based on thermogravimetric analysis (TGA) of the precursor in synthetic air (21% O_2, balance N_2) from room temperature to 1000 °C; similar values have been reported in the literature.[63] The pH of the solution was adjusted to 6 using $NH_3{\cdot}H_2O$ (28% NH_3 in H_2O, ≥ 99.99%—MilliporeSigma). The solution was dried and combusted on a hot plate at 540 °C, and the obtained raw ash was first ground with a mortar and pestle, and then, it was calcined at 950 °C for 4 h in ambient air to form the final perovskite structure using a heating and cooling rate of 5 °C/min.

La_2O_3 powder was purchased from MilliporeSigma (99.999%) and was used as received without any modification or pre-treatment.

2.2. Preparation of Dense BFZ91 Pellets for OCM Measurements. To prepare dense, disk-shaped BFZ91 pellets for OCM measurements, the calcined powder was mixed with 3 wt % polyvinyl butyral (acting as a binder) and ethanol and the mixture was homogenized in a mortar using a pestle. After ethanol evaporated, the powder-binder mixture was pressed uniaxially at 12 MPa in a cylindrical die to form the green body which was densified by sintering in ambient air at 1200 °C for 8 h using heating and cooling rates equal to 3 °C/min. The sintered pellets had a final diameter of D ≃ 16 mm and were then polished to the final thickness using silicon carbide sandpapers of different grit sizes until a smooth, mirror-like surface was obtained. The density of the final BFZ91 pellets was estimated using the Archimedes principle.

2.3. Button-Cell Reactor for OCM Measurements. Experimental measurements were obtained using a button-cell reactor shown in Supporting Information Figure S1. Additional information about the experimental setup is provided in the Supporting Information (Section 1) and in a previous work.[64] For the OCM measurements, 0.1 g of La_2O_3 powder were deposited on the CH_4 side of the BFZ91 membrane to create a fixed-bed type configuration, as shown in Supporting Information Figure S2.

Prior to any measurements, the reactor temperature was increased to 1025 °C with ambient air flowing in the air side (200 sccm) and pure argon (Ar) in the CH_4 side (100 sccm) and was maintained at these conditions overnight. This heat treatment is required to soften the gold rings so that they can attach well on the alumina tubes and on the membrane, thus ensuring a gas-tight system with minimized leaks. For all the experiments reported herein, the nitrogen (N_2) mole fraction at the exit of the CH_4 side of the reactor was below 0.1%, demonstrating that air leaks are negligible and do not affect the measurements.

To estimate J_{O_2}, C_{CH_4}, O_2 conversion (C_{O_2}), C_2 selectivities, yields, and activities, measurements of species mole fractions at the inlet and outlet of the CH_4 side are used as the input to a mole balance system of equations. All relevant equations are reported in the Supporting Information (Section 2). To understand the role of gas phase and surface reactions because of the presence of the BFZ91 membrane and La_2O_3 catalyst, measurements using an alumina microprobe with outer and inner diameters equal to 1.6 and 0.8 mm, respectively, were conducted near the membrane surface (approximately 1 mm away) and within the La_2O_3 bed. Silica was used as a desiccant material to remove any H_2O from the mixture prior to introduction into the gas chromatograph (GC) for analysis. To estimate the mole fraction of H_2O near the membrane surface (but still in the gas phase), a carbon to hydrogen atom balance between that location and the CH_4 side inlet was used.[29] Then, the GC measurements were corrected to estimate the true (i.e., on a wet basis) mole fraction of species within the reactor.[29] The system of equations is reported in the Supporting Information (Section 3). Experimental uncertainties are included in all plots; to highlight this, data are plotted using open markers. All species mole fractions reported in this work are plotted on a wet basis, that is, accounting for H_2O in the mixture.

2.4. Material Characterization. The X-ray diffraction (XRD) patterns of the as-prepared, as-received, and used materials were obtained at room temperature with a PANalytical X'Pert Pro diffractometer using copper (Cu) Kα radiation

https://dx.doi.org/10.1021/acscatal.0c04888
ACS Catal. 2021, 11, 3638−3661

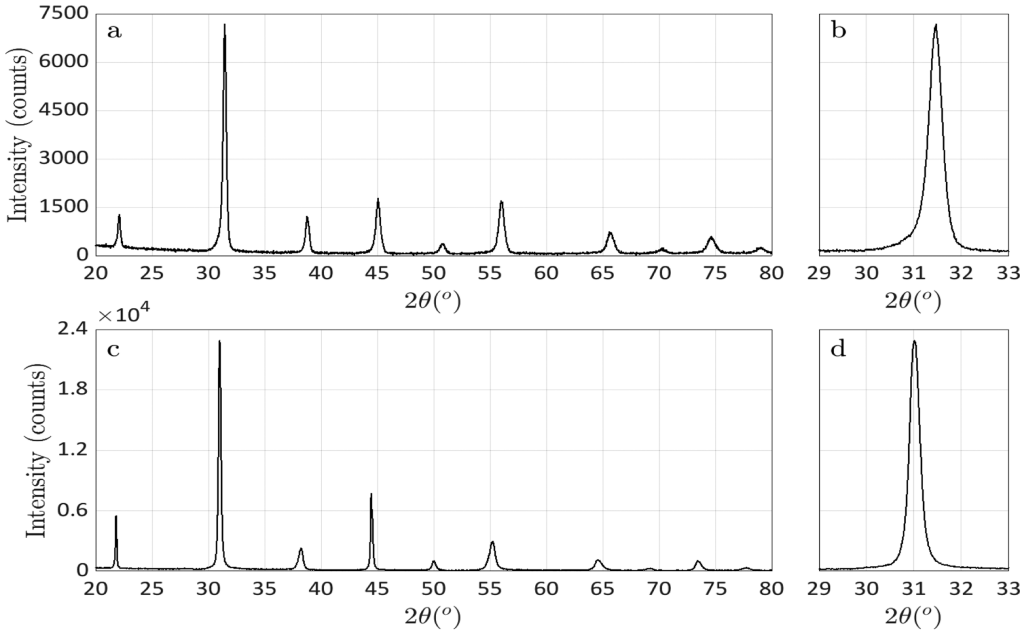

Figure 1. Comparison between the XRD pattern of the calcined BFZ91 powder (a,b) and that of the sintered BFZ91 pellet (c,d) prior to polishing. Subplots b and d zoom into the 2θ range of 29−33° to highlight the peak shift between the two patterns.

Table 1. Crystal Structure, Space Group, Lattice Constants and Phase Identification for: (1) the Calcined BFZ91 Powder (950 °C for 4 h), (2) the As-Prepared Dense BFZ91 Pellet (1200 °C for 8 h), (3) the As-Received La_2O_3 Powder, and (4) the As-Received La_2O_3 Powder after Heat-Treatment in Ambient Air at 800 °C for 2 h

no.	material	phases	crystal structure	space group	lattice constants (Å)	phase %
1	calcined BFZ91 powder	$BaFe_{0.9}Zr_{0.1}O_{2.785}$	cubic	$Pm\bar{3}m$	$a = b = c = 4.022$	100.0
2	as-prepared BFZ91 pellet	$BaFe_{0.9}Zr_{0.1}O_{2.636}$	cubic	$Pm\bar{3}m$	$a = b = c = 4.079$	100.0
3	as-received La_2O_3 powder	La_2O_3	hexagonal	$P\bar{3}m1$	$a = b = 3.937$, $c = 6.130$	97.3
		$La(OH)_3$	hexagonal	$P6_3/m$	$a = b = 6.538$, $c = 3.589$	2.7
4	La_2O_3 powder heat-treated at 800 °C	La_2O_3	hexagonal	$P\bar{3}m1$	$a = b = 3.937$, $c = 6.129$	100.0

operating at voltage and current equal to 45 kV and 40 mA, respectively. The patterns were recorded in the 2θ range of 20−80° and were analyzed using the software HighScore Plus. The same software was also used for phase identification and Rietveld refinement. Scanning electron microscopy (SEM) and energy-dispersive X-ray spectroscopy (EDS) were conducted using a Zeiss Merlin high-resolution scanning electron microscope. TGA measurements were conducted using a Q50 thermal analyzer from TA Instruments. Buoyancy corrections were included by repeating the TGA measurements at identical conditions using an empty sample pan. To estimate the surface area of the powder materials, the Brunauer−Emmett−Teller (BET) method was employed using a ASAP 2020 surface area analyzer from Micromeritics. To remove any moisture, the samples were degassed at T = 150 °C for 30 min in vacuum prior to BET measurements. BET was conducted in N_2 and two measurements were performed for each material with a sample mass equal to ∼0.5 g.

3. RESULTS AND DISCUSSION

3.1. Characterization of the As-Prepared BFZ91 Powder and Pellet. It is known that the $BaFeO_{3-\delta}$ parent perovskite exhibits a hexagonal crystal structure at room temperature,[65,66] but the structure changes to triclinic at 700 °C and then to cubic at 900 °C when exposed to air.[66,67] High J_{O_2} is achieved at temperatures exceeding 750 °C, that is, when $BaFeO_{3-\delta}$ obtains a triclinic or cubic phase.[66,67] Given that phase transitions during heating and cooling could lead to mechanical failure of the dense membrane because of volume changes, phase stabilization is required by appropriate doping. The addition of 2−10% of Zr in the B-site of $BaFeO_{3-\delta}$ can eliminate the aforementioned phase transition, giving rise to a cubic crystal structure at room temperature.[65] When the Zr doping increases to 15%, secondary phases appear demonstrating that the solubility limit of Zr in $BaFeO_{3-\delta}$ is less than 15%.[65]

Supporting Information Figure S3 shows the XRD patterns of the BFZ91 powder before and after calcination at high temperature; the latter is also shown in Figure 1a. The XRD pattern of the uncalcined powder (i.e., raw ash) is composed of several peaks that correspond to the intermediate phases of the solid solution. Calcination in ambient air at 950 °C for 4 h activates cation diffusion and leads to the formation of a phase pure perovskite oxide. The calcined BFZ91 powder exhibits a cubic crystal structure in the $Pm\bar{3}m$ space group without any secondary phases. The diffraction pattern agrees with that of $BaFe_{0.95}Zr_{0.05}O_{2.56}$ (ICDD 04-022-8935)[68] and is in agreement with a previous work on Zr-doped $BaFeO_{3-\delta}$ oxides.[57,65−67] High-temperature XRD measurements for BFZ91 in ambient air have also shown that the cubic structure is preserved up to 950 °C.[57] The surface area of the calcined BFZ91 powder was estimated at 4.0 ± 0.3 m^2/g using BET.

Figure 1 compares the XRD pattern of the calcined BFZ91 powder with that of the sintered BFZ91 pellet prior to any polishing. As expected, the crystallization of the BFZ91 pellet

https://dx.doi.org/10.1021/acscatal.0c04888
ACS Catal. 2021, 11, 3638−3661

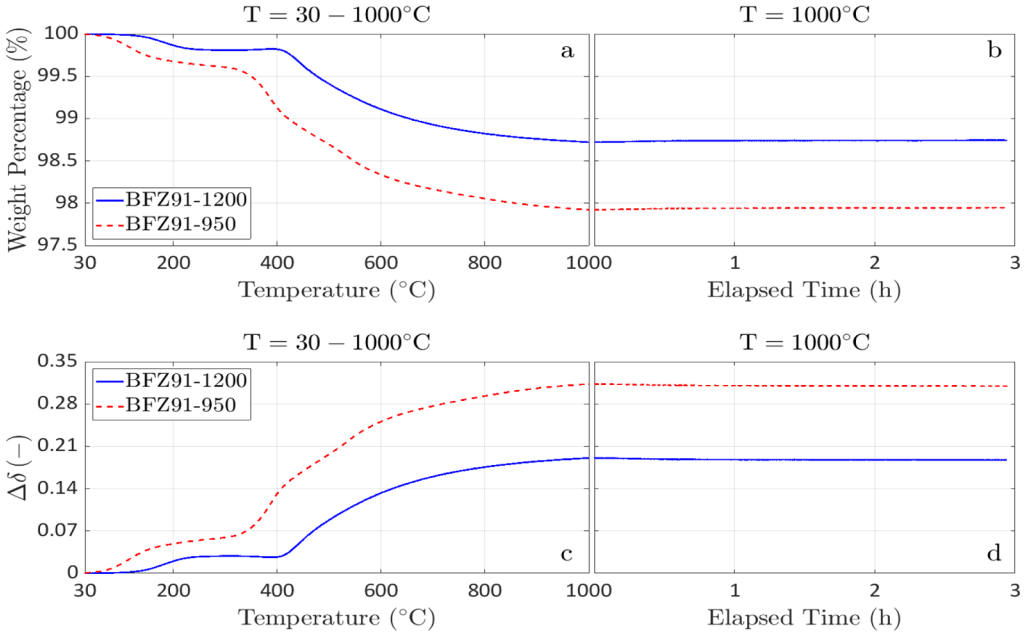

Figure 2. TGA measurements in ambient air (100 sccm) between T = 30−1000 °C for BFZ91-950 (red dashed line) and BFZ91-1200 (blue solid line). (a) Weight percentage during the heating step, (b) weight percentage during equilibration at 1000 °C for 3 h, (c) $\Delta\delta$ during the heating step, and (d) $\Delta\delta$ during equilibration at 1000 °C for 3 h.

increases because of sintering at 1200 °C. This is confirmed by the increase in the peak intensity and the decrease in the peak width as compared to the peaks of the calcined BFZ91 powder. The crystal structure of the BFZ91 pellet remains cubic (space group $Pm\bar{3}m$) and no secondary phases are detected. An interesting observation is that the peak positions of the sintered BFZ91 pellet shift to lower 2θ angles when compared to the peak positions of the calcined BFZ91 powder. This is highlighted in Figure 1 (subplots b and d), which zoom into the 2θ range of 29−33°. This peak shift toward lower 2θ angles implies a unit cell lattice expansion for the sintered BFZ91 pellet compared to the unit cell of the calcined BFZ91 powder. Rietveld refinement was used to estimate the lattice constant of each pattern, and the results are shown in Table 1, confirming the aforementioned lattice expansion of the BFZ91 pellet ($a = b = c = 4.079$ Å) compared to that of the BFZ91 powder ($a = b = c = 4.022$ Å).

Interestingly, the oxygen content of the BFZ91 powder and pellet estimated based on the Rietveld refinement is different (Table 1). Although iodometric titration is a more accurate method to evaluate the oxygen deficiency (δ) of each material,[68] the fact that less oxygen is estimated in the structure of the BFZ91 pellet suggests that the source of the lattice expansion of the BFZ91 pellet could be related to an irreversible loss of oxygen because of sintering at 1200 °C. This is consistent with the tendency of ceramic oxides to lose oxygen from their structure when the temperature is increased and as a function of P_{O_2}. To support our hypothesis, we conducted TGA measurements with: (1) the calcined BFZ91 powder (950 °C, 4 h), which will be denoted BFZ91-950, and (2) the BFZ91-950 powder recalcined at 1200 °C for 8 h, that is, using the same heat treatment employed during the sintering of a BFZ91 pellet; this powder will be denoted BFZ91-1200. For the TGA measurements, approximately 0.1 g of powder were first heated from room temperature to 150 °C for 2 h to ensure the investigated materials were dehydrated. Then, the temperature was decreased to 30 °C until mass equilibration. After this step, the TGA furnace was heated from 30 to 1000 °C using a heating rate equal to 20 °C/min followed by equilibration at 1000 °C for 3 h. Ambient air at 100 sccm was flowing continuously during the measurements. The results are shown in Figure 2 (the dehydration step is not plotted), which also includes the oxygen deficiency change ($\Delta\delta$) calculated using the following equation:

$$\Delta\delta = \frac{W_{BaFe_{0.9}Zr_{0.1}O_{3-\delta}}}{W_O}\frac{\Delta m}{m_s} \tag{3}$$

In eq 3, $W_{BaFe_{0.9}Zr_{0.1}O_{3-\delta}}$ is the molar weight of the off-stoichiometric $BaFe_{0.9}Zr_{0.1}O_{3-\delta}$ material at room temperature (calculated using the stoichiometry defined in Table 1 for each sample), Δm is the change in the sample's mass during the TGA measurement, m_s is the sample's starting mass, and W_O is the atomic weight of oxygen. Figure 2 indeed shows that the oxygen loss is different in the studied powders throughout the entire heating step with BFZ91-950 losing more oxygen compared BFZ91-1200. As a result, $\Delta\delta$ is higher for BFZ91-950 compared to BFZ91-1200. Note that the calculated $\Delta\delta$ values, as shown in Figure 2, are in agreement with TGA measurements conducted in air for $BaFe_{0.95}Zr_{0.05}O_{2.56}$.[68] In that work, however, the lattice expansion observed here was not reported. Based on the XRD and TGA results, as shown in Figures 1 and 2, respectively, we suggest that the lattice expansion of the BFZ91 pellet is because of an irreversible increase in the content of oxygen vacancies induced by the sintering at high temperatures.

We note here that although the XRD and TGA results shown in Figures 1 and 2, respectively, confirm a lattice expansion induced by sintering at higher temperatures, the lattice expansion is not related only with changes in the amount of oxygen in the structure but also because of changes in the amount of the iron (Fe) charged species within the material. To further elaborate on this, we postulate the following point defect chemistry model for BFZ91 written using the Kröger−Vink notation:[28,29,58]

https://dx.doi.org/10.1021/acscatal.0c04888
ACS Catal. 2021, 11, 3638−3661

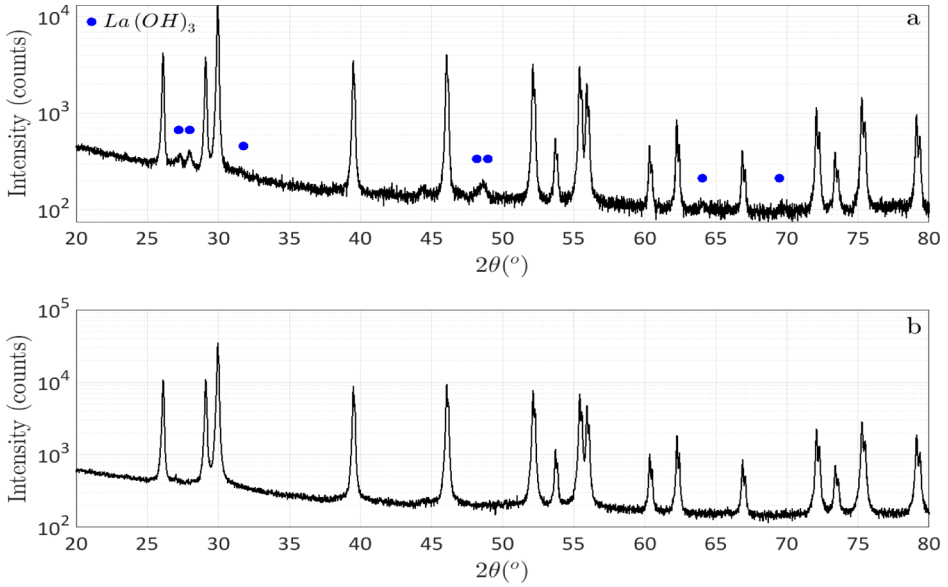

Figure 3. XRD patterns of: (a) as-received La_2O_3 powder and (b) as-received La_2O_3 powder after heat-treatment in ambient air at 800 °C for 2 h. Blue circles correspond to $La(OH)_3$ peaks (ICDD 04-016-2506). Note that a logarithmic *y*-axis is used to increase the visibility of the $La(OH)_3$ peaks.

$$\frac{1}{2}O_2(g) + V_O^{\bullet\bullet} + 2Fe_{Fe}^{x} \rightleftharpoons O_O^{x} + 2Fe_{Fe}^{\bullet} \quad (4)$$

$$2Fe_{Fe}^{x} \rightleftharpoons Fe_{Fe}^{\bullet} + Fe_{Fe}^{\prime} \quad (5)$$

Reaction 4 reflects the O_2 incorporation into the material while reaction 5 accounts for the Fe disproportionation. A similar point defect model has been proposed for other materials.[28,29,58,69,70] In reactions 4 and 5, $V_O^{\bullet\bullet}$ denotes an oxygen vacancy, O_O^{x} is an oxygen ion (O^{2-}) incorporated into an O^{2-} lattice site while $Fe_{Fe}^{\bullet}$, Fe_{Fe}^{x}, and $Fe_{Fe}^{\prime}$ correspond to Fe^{+4}, Fe^{+3}, and Fe^{+2} incorporated into the Fe^{+3} lattice site, respectively. $Fe_{Fe}^{\bullet}$, Fe_{Fe}^{x}, and $Fe_{Fe}^{\prime}$ participate in the electron transfer required to ionize O_2 prior to incorporation into the material. Depending on the BFZ91 defect chemistry and thermodynamics, O_2 incorporation may also happen because of the following reaction, which is the combination of reactions 4 and 5:[69,70]

$$\frac{1}{2}O_2(g) + V_O^{\bullet\bullet} + 2Fe_{Fe}^{\prime} \rightleftharpoons O_O^{x} + 2Fe_{Fe}^{x} \quad (6)$$

Although determining the exact defect chemistry and thermodynamics of BFZ91 is outside the scope of this investigation and will be addressed in our future work, the proposed point defect model allows for a deeper understanding of the observed chemical expansion phenomenon and its implications on the properties of the investigated materials. The mass loss, as shown in Figure 2, is because of oxygen release from the material leaving behind oxygen vacancies. According to reactions 4−6, this should be accompanied by a change in the concentration of the different Fe states ($Fe_{Fe}^{\bullet}$, Fe_{Fe}^{x}, and $Fe_{Fe}^{\prime}$) dictated by the thermodynamics of reactions 4−6, the $ABO_{3-\delta}$ stoichiometry, and the conservation of charge neutrality in the bulk of the material. This means that BFZ91-950 and BFZ91-1200 have different amounts of oxygen vacancies in their structure as well as different concentrations of Fe states. Besides having an impact on the final unit cell volume (as the different Fe states are characterized by a different ionic radius), the different concentrations of the charged species are expected to affect the kinetics of reactions 4−6, and the diffusion of charged species within the material. As a result, this phenomenon becomes very important when calculating properties of materials (e.g., electronic and ionic conductivity, oxygen deficiency as a function of T and P_{O_2} etc.) confirming that for some materials, the heat treatment history can play a significant role in the measured properties. Obviously, an irreversible chemical expansion due to heat treatment may not be observed for other materials; but to improve consistency, material properties should be obtained using samples with the same heat treatment history as the material to be investigated in the final application.

Lastly, based on the estimated unit cell of the sintered BFZ91 pellet, the theoretical density of BFZ91 is calculated as $\rho_{BFZ91}^{theoretical}$ = 5.845 g/cm^3 and agrees with other studies.[64] The true density of the sintered BFZ91 pellets (estimated using the Archimedes principle) was equal to $\rho_{BFZ91}^{true} \approx 5.840$ g/cm^3, which corresponds to a 99.9% relative density, demonstrating that fully dense BFZ91 membranes were successfully fabricated in this work.

3.2. Characterization of the As-Received La_2O_3 Powder. Commercial La_2O_3 powder was used in the current investigation as the OCM catalyst. The La_2O_3 powder was used in OCM experiments as-received, that is, without any additional treatment. The surface area of the as-received La_2O_3 powder estimated using BET was 3.0 ± 0.7 m^2/g.

To investigate the crystal structure of the as-received La_2O_3 powder, XRD is conducted, and Figure 3a shows the corresponding pattern. Interestingly, the as-received La_2O_3 powder is not phase pure. Although the main peaks can be assigned to the hexagonal La_2O_3 phase (ICDD 04-005-4229), there are 7 additional peaks at 2θ angles equal to 27.3, 28.0, 31.6, 48.2, 48.6, 64.0, and 69.5°. All 7 peaks match very well with the high intensity peaks of the hexagonal lanthanum hydroxide ($La(OH)_3$) phase (ICDD 04-016-2506). Using Rietveld refinement, we estimated that the secondary $La(OH)_3$ phase corresponds to 2.7% of the powder with the remaining being La_2O_3. The crystal structure data are reported in Table 1.

Although the amount of the secondary $La(OH)_3$ phase is low, it is worth understanding its origin as well as its potential decomposition at higher temperatures because the presence of this phase could potentially affect the OCM activity of the

https://dx.doi.org/10.1021/acscatal.0c04888
ACS Catal. 2021, 11, 3638−3661

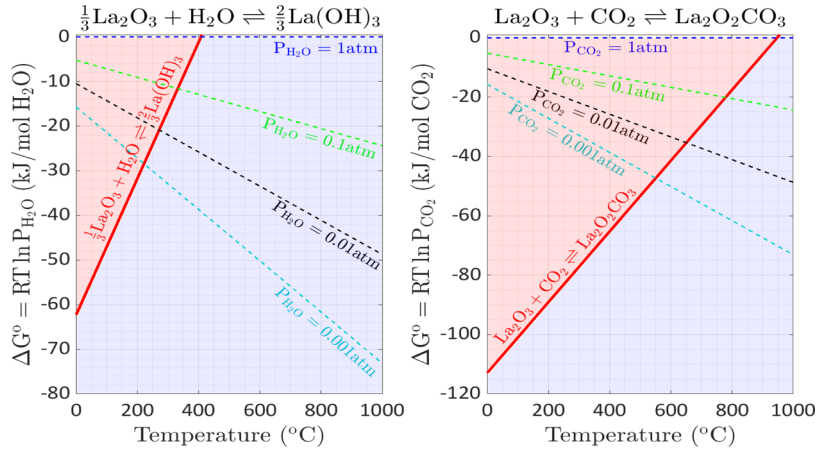

Figure 4. Ellingham diagrams showing the stability of $La(OH)_3$ (left) and $La_2O_2CO_3$ (right) as a function of T and P_{H_2O} or P_{CO_2} (for absolute pressure of 1 atm). The light pink zone denotes the area of $La(OH)_3$ and $La_2O_2CO_3$ formation, while the light blue zone denotes the area of La_2O_3 formation. The red solid line denotes the standard-state Gibbs free energy change of the corresponding reaction ($\Delta G^\circ = \Delta H^\circ - T\Delta S^\circ$). The dashed lines correspond to the standard-state Gibbs free energy change as a function of T for a fixed partial pressure ($\Delta G^\circ = RT \ln P_{H_2O}$ or $\Delta G^\circ = RT \ln P_{CO2}$). Standard-state molar enthalpies of formation and standard-state molar entropies for each species were obtained from reference tables.[77,79−81]

catalyst. We suspect that the source of $La(OH)_3$ is the hydroxylation of La_2O_3 with H_2O from ambient air as this reaction has been shown to occur at room temperature.[71] In the presence of an inert gas, $La(OH)_3$ decomposes to lanthanum hydroxide oxide (LaOOH) and then to La_2O_3 through the following two-step mechanism:[72]

$$La(OH)_3 \rightarrow LaOOH + H_2O \quad (7)$$

$$2LaOOH \rightarrow La_2O_3 + H_2O \quad (8)$$

Kinetically, the formation of LaOOH through reaction 7 happens at $T \approx 330$ °C while full dehydration to La_2O_3 via reaction 8 takes place at $T \approx 490$ °C.[72] At $T = 550$ °C, XRD results show that pure La_2O_3 is obtained.[72] However, the aforementioned decomposition mechanism changes in the presence of CO_2 given that lanthanum is a basic element, and hence, its oxides and hydroxides can easily form lanthanum dioxycarbonate ($La_2O_2CO_3$) or other carbonate species. The decomposition of $La(OH)_3$ in ambient air proceeds through the following mechanism:[73,74]

$$2La(OH)_3 + CO_2 \rightarrow La_2O_2CO_3 + 3H_2O \quad (9)$$

$$La_2O_2CO_3 \rightarrow La_2O_3 + CO_2 \quad (10)$$

Reaction 9 takes place between $T = 200$−600 °C, while reaction 10 happens at high rates in the interval $T = 650$−800 °C.[73] XRD results reported in the literature confirm the presence of $La_2O_2CO_3$ at 500−700 °C during the process of $La(OH)_3$ decomposition in air,[73,75] while pure La_2O_3 is observed at 800 °C.[75] This is consistent with additional data showing that reaction 10 is triggered at $T \approx 700$−725 °C.[76−78] To further confirm the aforementioned literature results, we have heat treated the as-received La_2O_3 powder in ambient air at 800 °C for 2 h. As shown in Figure 3b, XRD results obtained immediately after this heat treatment confirm that a pure phase La_2O_3 material can be obtained without any additional $La(OH)_3$ or $La_2O_2CO_3$ phases. To facilitate the discussion in the following sections, Figure 4 shows the stability of $La(OH)_3$ and $La_2O_2CO_3$ as a function of T and P_{H_2O} or P_{CO_2}. Regarding the T at which decomposition to La_2O_3 occurs for a fixed partial pressure, the differences between the results in Figure 4 and the literature results presented earlier are because the former provide information from a purely thermodynamic point of view while the latter are based on TGA measurements for which the kinetics of the reactions are also considered.

Based on the aforementioned discussion, the following important conclusions are drawn. First, although the as-received La_2O_3 powder contains a small amount of $La(OH)_3$, the latter decomposes to pure La_2O_3 during the initial heating of the button-cell reactor in pure Ar from room temperature to 1025 °C (see Section 2.3 and Figure 4). After sealing is completed, the reactor temperature decreases to $T = 750$ °C while pure Ar is still flowing on the CH_4 side. OCM experiments begin at $T = 750$ °C or $T = 850$ °C, and hence, the starting OCM catalyst is expected to be pure La_2O_3 without any secondary phases. This is consistent with a previous work on undoped and Sr-doped La_2O_3 where pretreatment in pure N_2 at 800 °C was conducted prior to OCM experiments to remove such impurities.[60] Second, although it is thermodynamically favorable for lanthanum hydroxides and carbonates to decompose at $T > 725$ °C, we stress that this happens in the presence of air or an inert gas. As shown in Figure 4, at a fixed T, the partial pressure of H_2O and CO_2 can alter the tendency toward the formation of lanthanum hydroxides or carbonates. Under OCM conditions, the gaseous environment will include species such as CH_4, O_2, H_2O, CO_2, C_2 and so forth. Depending on their concentrations, new lanthanum-based phases may appear, which could have beneficial or deleterious effects on the C_2 production. For example, $La_2O_2CO_3$ rods have been shown to be active for OCM at low temperatures (420−500 °C) when prepared using a hydrothermal method but low OCM activity was observed for $La_2O_2CO_3$ plates synthesized via a precipitation method.[78]

The thermodynamics of the aforementioned lanthanum-containing species create another challenge regarding the characterization of the used La_2O_3 catalyst. After the end of the OCM measurements, cooling down the reactor from $T \geq 750$ °C to room temperature can happen in two ways: (1) by flowing pure Ar in the CH_4 side of the reactor and (2) by flowing CH_4−Ar mixtures. In the first scenario, if lanthanum hydroxides or carbonates form on La_2O_3 during OCM (because of exposure to a hydrocarbon environment), cooling down the reactor in pure Ar will lead to their decomposition, and hence, these phases

https://dx.doi.org/10.1021/acscatal.0c04888
ACS Catal. 2021, 11, 3638−3661

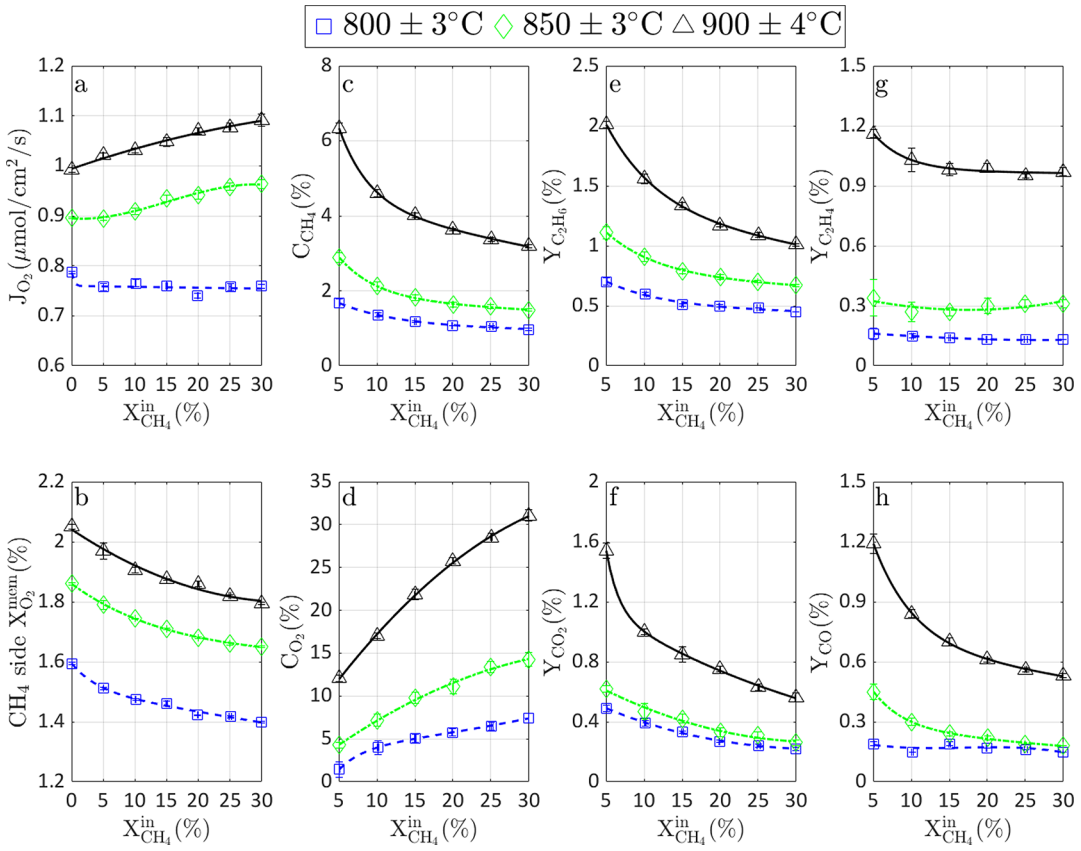

Figure 5. Performance of BFZ91 as a function of T and $X^{in}_{CH_4}$ in the absence of La_2O_3. (a) J_{O_2}, (b) CH_4 side $X^{mem}_{O_2}$, (c) C_{CH_4}, (d) C_{O_2}, (e) $Y_{C_2H_6}$, (f) Y_{CO_2}, (g) $Y_{C_2H_4}$, and (h) Y_{CO}. Color marker-line equivalence: (1) $T = 800 \pm 3$ °C: blue squares-dashed line, (2) $T = 850 \pm 3$ °C: green diamond-dashed dotted line, and (3) $T = 900 \pm 4$ °C: black triangles-solid line. Lines are guides to the eye. During the experiment, ambient air was flowing in the air side at $\dot{Q}_{air} = 200$ sccm while CH_4–Ar mixtures with $\dot{Q}^{total}_{CH_4-Ar} = 100$ sccm were introduced in the CH_4 side. The thickness of the membrane was 0.67 mm.

may not be detected by common characterization methods such as XRD although they may still form under the OCM conditions reported in this work. If the second option is employed, then, as will be shown in the next section, species such as H_2O or CO_2 will still form through CH_4 full oxidation because of the finite O_2 permeation through the membrane. These will react with La_2O_3 at $T < 725$ °C forming lanthanum hydroxides or carbonates. These phases may be detected by XRD, but they will correspond to phases formed during the cooling of the reactor rather than under the OCM conditions of our work. Cooling down the reactor by flowing an inert gas in the feed side (instead of air) could solve the aforementioned problem, but then, the presence of CH_4 in the stream will decompose the BFZ91 membrane. In our work, we have chosen to cool down the reactor using ambient air in the air side and 5% CH_4 (balanced with Ar) in the CH_4 side in order to preserve the structure of the BFZ91 membrane and reduce the impact of CH_4 and its gaseous products on the final La_2O_3 crystal structure.

As a final remark, note that the aforementioned challenge demonstrates once again the implications of properly characterizing OCM catalysts with ex situ techniques and highlights the importance of using in situ catalyst characterization methods. Similar conclusions have been drawn for La_2O_3 investigated ex situ using X-ray photoelectron spectroscopy after OCM measurements.[82]

3.3. CH_4 Conversion Using BFZ91 in the Absence of a Catalyst. To determine the species produced by the reaction of CH_4 with O_2 that permeates through BFZ91 and to identify any catalytic reactions taking place on BFZ91, we begin our analysis with experiments conducted in the absence of a catalyst on the CH_4 side of BFZ91. These reference measurements are taken in the range $T = 800$–900 °C and $X^{in}_{CH_4} = 0 - 30\%$.

Figure 5a shows that at $T = 800$ °C, $J_{O_2} \approx 0.75$ (μmol/cm²/s), and it is almost constant in the range $X^{in}_{CH_4} = 0 - 30\%$. However, at $T = 850$ °C and $T = 900$ °C, J_{O_2} rises as more CH_4 is added into the stream. This dependency is related to the rate-limiting step of the O_2 permeation mechanism.[28−31] It is known that in CMRs, J_{O_2} is limited by surface reactions on either gas−membrane interface or by bulk diffusion. In the presence of a fuel, its reaction with O_2 from the membrane can increase J_{O_2} if surface reactions on the fuel side are not rate limiting. This is because of a decrease in the fuel side μ_{O_2} leading to an overall increase in the μ_{O_2} gradient between the two membrane sides.[29,64,83,84] Previous work has shown that BFZ91 exhibits thickness limitations, and hence, higher J_{O_2} can be achieved using thinner membranes.[67] However, for a fixed thickness, BFZ91 also shows limitations on the CH_4 side gas−membrane interface.[57,58] The results in Figure 5a suggest that at $T = 800$ °C, the CH_4 side surface reaction is limiting J_{O_2} in addition to the bulk diffusion resistance. As T rises, surface reactions are accelerated, and hence, the addition of CH_4 increases J_{O_2} when

https://dx.doi.org/10.1021/acscatal.0c04888
ACS Catal. 2021, 11, 3638−3661

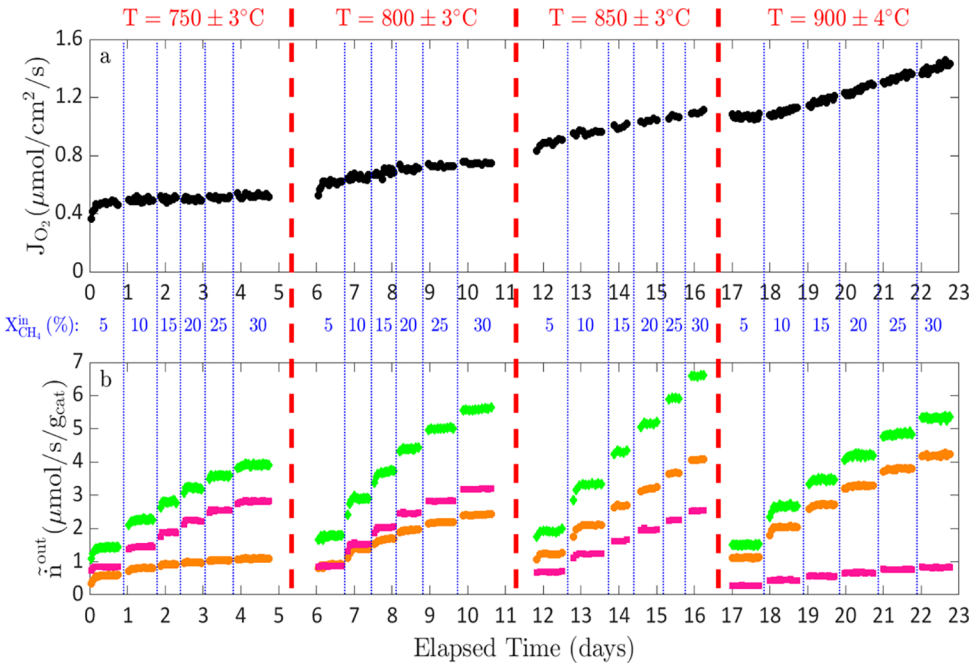

Figure 6. Long-term OCM measurements of BFZ91 with La_2O_3 powder on the CH_4 side. (a) J_{O_2} (black) as a function of time and (b) $\tilde{n}^{out}_{C_2H_4}$ (orange), $\tilde{n}^{out}_{C_2H_6}$ (pink) and $\tilde{n}^{out}_{C_2} = \tilde{n}^{out}_{C_2H_6} + \tilde{n}^{out}_{C_2H_4} + \tilde{n}^{out}_{C_2H_2}$ (green) as a function of time. Red dashed lines correspond to increases in the reactor temperature while blue dotted lines correspond to instants of $X^{in}_{CH_4}$ change. Measurements were conducted every 1 h. During the experiment, ambient air was flowing in the air side at $\dot{Q}_{air}$ = 200 sccm while CH_4–Ar mixtures with $\dot{Q}^{total}_{CH_4-Ar}$ = 100 sccm were introduced in the CH_4 side. The thickness of the membrane was 0.68 mm, while the thickness of the La_2O_3 catalyst layer was 1.5 mm.

compared to the nonreactive case. This effect is more pronounced at 850 and 900 °C.

As shown in Figure 5c,d, at T = 800 °C, $C_{CH_4} < 2\%$ while $C_{O_2} < 8\%$. At higher T and for the same $X^{in}_{CH_4}$, both C_{CH_4} and C_{O_2} increase, consistent with enhanced reactivity at elevated T. However, for the same T, C_{CH_4} decreases as more CH_4 is added into the stream; C_{O_2} increases but does not reach 100%, a sign that under the conditions investigated herein, CH_4 cannot fully convert all the available O_2 into products in the presence of BFZ91. In addition, Figure 5b and Supporting Information Figure S4 show that for all cases, the CH_4 side $X^{mem}_{O_2}$ and $X^{out}_{O_2}$ are high, further confirming that CH_4 does not react with O^x_O or gaseous O_2 at considerable rates (especially at lower T) and that a low P_{O_2} environment cannot be established when using BFZ91 alone. According to Supporting Information Figure S4, some fraction of the fuel succeeds to react with lattice oxygen on the BFZ91 surface or with molecular O_2 in the gas phase, as demonstrated by the nonzero mole fraction of C_2H_6, C_2H_4, H_2O, CO_2, H_2, and CO. The production of these species, however, is low, as confirmed by the low yields shown in Figure 5e–h and in Supporting Information Figure S5. For comparison, the results of the same experiment in the presence of La_2O_3 (shown in Section 3.5) reveal negligible O_2 near the CH_4 side of the membrane, $C_{O_2} \approx 100\%$ and higher C_2 yields.

The aforementioned results lead us to the following important conclusions. First, it appears that the BFZ91 membrane does not have a strong catalytic activity toward the decomposition or oxidation of CH_4. This is a notable property of the BFZ91 membrane, which is expected to increase the C_2 yields by avoiding side reactions of CH_4 producing species other than C_2H_6 and C_2H_4. Second, according to Figure 5e,g and Supporting Information Figure S5, some activity toward the production of C_2 is observed. For example, $S_{C_2H_6}$ is between 30–50% while that of $S_{C_2H_4}$ is around 10–30%. However, the corresponding yields are below 2%. Although a C_2 yield of ~3% can be obtained at 900 °C, the use of an OCM-active catalyst is expected to promote C_2 production at lower T. The same results confirm that overall, the role of the BFZ91 membrane is to supply O_2 from the air side without a significant participation in the conversion of CH_4. Third, according to Supporting Information Figure S4, the mixture composition near the membrane surface can be different compared to that at the outlet of the reactor. In addition to gaseous diffusion, gas phase chemistry can alter the mixture composition along the hot zone of the reactor when using a fuel. Hence, measuring the concentration of species near the membrane surface in addition to the outlet of the reactor is required to understand the effect of gas phase reactions, and the impact of the membrane and catalyst on the fuel conversion.

We note here that each experimental point, as shown in Figure 5, is recorded after a stabilization period of approximately 1 day. No loss of activity was observed for the entire duration of the experiment. This is confirmed by the XRD results, as shown in Supporting Information Figure S6. No secondary phases are observed in the XRD patterns of the BFZ91 membrane on both sides. The stability of BFZ91 is associated with the doping of Zr in the B-site of the perovskite which has been shown to improve the resistance to decomposition and the formation of carbonates when the material is exposed to a mixture of hydrocarbons.[33,57,58,85] Regarding the stability of BFZ91 in a CO_2-containing environment, we note that Balachandran et al. have

https://dx.doi.org/10.1021/acscatal.0c04888
ACS Catal. 2021, 11, 3638–3661

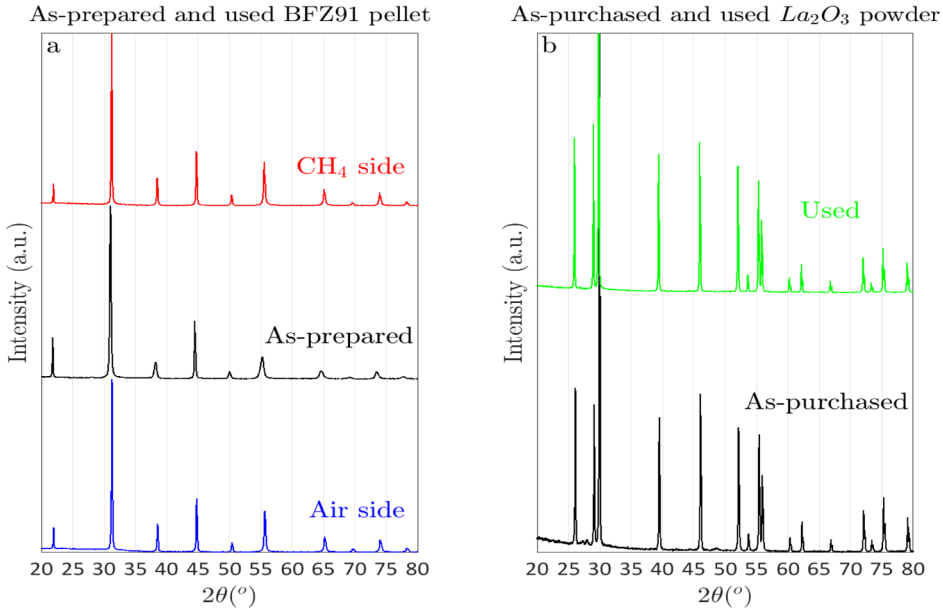

Figure 7. XRD patterns of: (a) as-prepared and used BFZ91 pellet and (b) as-received and used La_2O_3 catalyst. Patterns correspond to the long-term measurements reported in Figure 6.

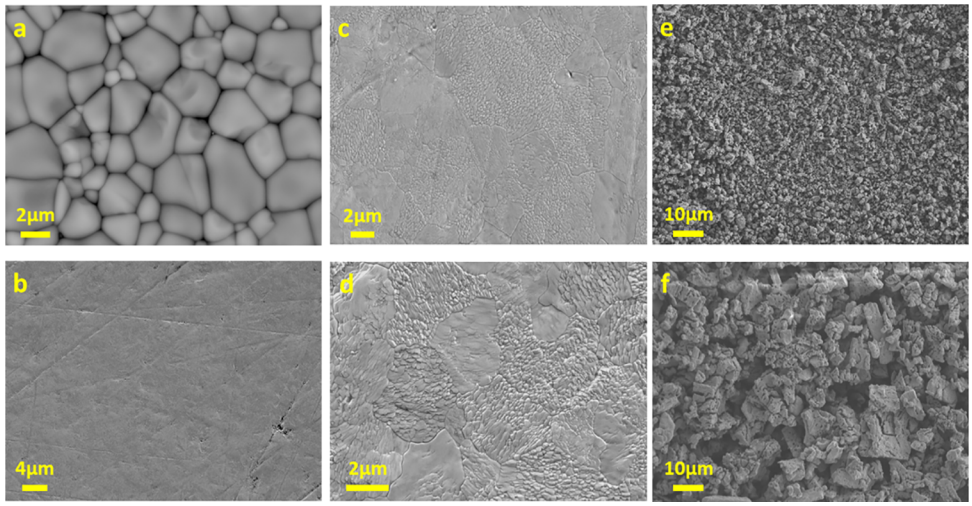

Figure 8. SEM images of BFZ91 and La_2O_3: (a) as-prepared BFZ91 pellet prior to polishing, (b) as-prepared BFZ91 pellet after polishing and prior to any measurements, (c) air side of the BFZ91 pellet after the end of the OCM measurements with La_2O_3, (d) CH_4 side of the BFZ91 pellet after the end of the OCM measurements with La_2O_3, (e) as-purchased La_2O_3 powder, and (f) La_2O_3 powder after the end of the OCM measurements.

already conducted studies using CO_2 mole fractions of 50 and 75% in the stream.[86] Although long-term studies were not reported, the obtained J_{O_2} was higher than LSCF membranes operating under the same conditions.[86] Because the formation of $BaCO_3$ is favorable at high T and CO_2, we would expect that any irreversible membrane deactivation at such conditions would have been immediate and would have lowered J_{O_2} significantly. However, more detailed studies (outside the scope of this work) are required to understand the high resistance of BFZ91 against $BaCO_3$ formation.

3.4. Performance and Stability of BFZ91 and La_2O_3 under Long-Term OCM Measurements. To evaluate the OCM performance of BFZ91 with La_2O_3, we conducted long-term measurements between T = 750−900 °C and $X^{in}_{CH_4} = 0 - 30\%$. During the experiment, the temperature was fixed and $X^{in}_{CH_4}$ increased to a specified value. Measurements were obtained every 1 h until the performance reached steady state. Once steady state was achieved, $X^{in}_{CH_4}$ increased again and the process was repeated. When the measurement at $X^{in}_{CH_4} = 30\%$ was completed, CH_4 was removed progressively and the temperature of the reactor increased to the next interval by flowing pure Ar in the CH_4 side. According to Figure 4 and the discussion in Section 3.2, this means that thermodynamically, the starting catalyst at each temperature was pure La_2O_3. Measurements were repeated in the same sequence for all the temperatures investigated here. The long-term measurements lasted for approximately 23 days after which we decided to stop the experiment. Note that Figure 6 only shows the reactive measurements; no stability was measured for $X^{in}_{CH_4} = 0\%$.

Figure 6 shows J_{O_2} and the activities of C_2H_6, C_2H_4, and C_2 (C_2H_6, C_2H_4, and acetylene (C_2H_2)) as a function of time,

https://dx.doi.org/10.1021/acscatal.0c04888
ACS Catal. 2021, 11, 3638−3661

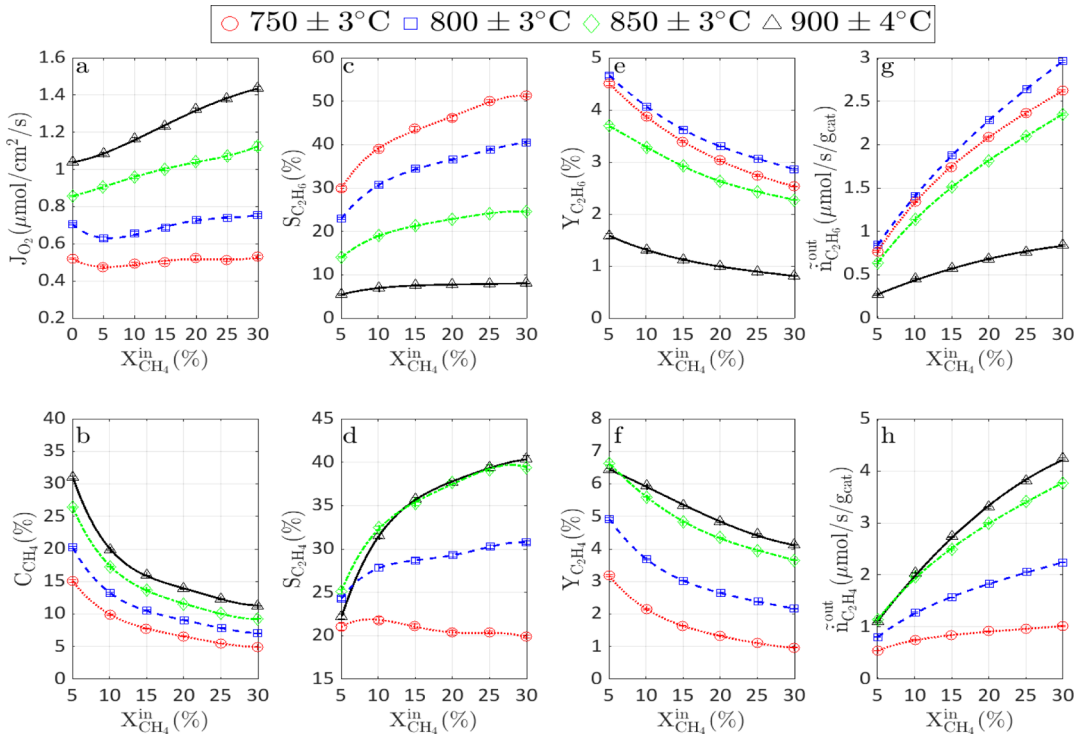

Figure 9. Steady-state OCM measurements of BFZ91 with La_2O_3 as a function of T and $X^{in}_{CH_4}$. (a) J_{O_2}, (b) C_{CH_4}, (c) $S_{C_2H_6}$, (d) $S_{C_2H_4}$, (e) $Y_{C_2H_6}$, (f) $Y_{C_2H_4}$, (g) $\tilde{n}_{C_2H_6}$, and (h) $\tilde{n}_{C_2H_4}$. Color marker-line equivalence: (1) $T = 750 \pm 3$ °C: red circles-dotted line, (2) $T = 800 \pm 3$ °C: blue squares-dashed line, (3) $T = 850 \pm 3$ °C: green diamonds-dashed dotted line, and (4) $T = 900 \pm 4$ °C: black triangles-solid line. Lines are guides to the eye. The thickness of the membrane was 0.68 mm, while the thickness of the La_2O_3 catalyst layer was 1.5 mm.

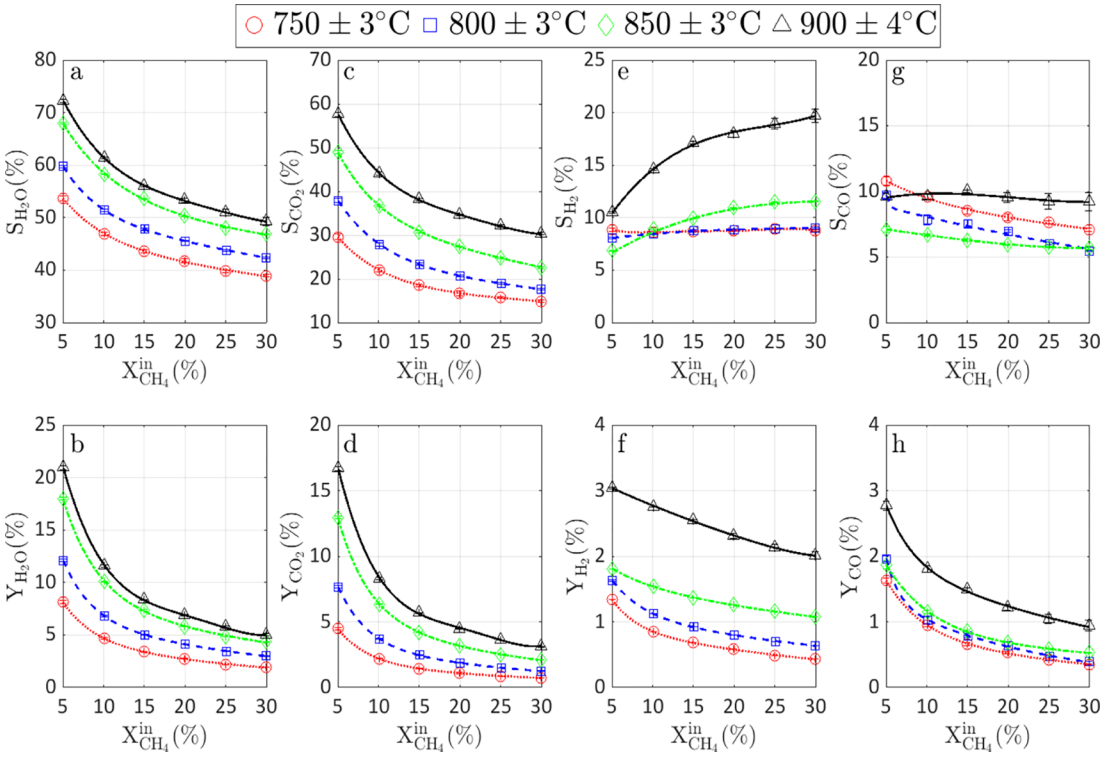

Figure 10. Steady-state OCM measurements of BFZ91 with La_2O_3 as a function of T and $X^{in}_{CH_4}$. (a) S_{H_2O}, (b) Y_{H_2O}, (c) S_{CO_2}, (d) Y_{CO_2}, (e) S_{H_2}, (f) Y_{H_2}, (g) S_{CO}, and (h) Y_{CO}. Color marker-line equivalence: (1) $T = 750 \pm 3$ °C: red circles-dotted line, (2) $T = 800 \pm 3$ °C: blue squares-dashed line, (3) $T = 850 \pm 3$ °C: green diamonds-dashed dotted line, and (4) $T = 900 \pm 4$ °C: black triangles-solid line. Lines are guides to the eye. The thickness of the membrane was 0.68 mm, while the thickness of the La_2O_3 catalyst layer was 1.5 mm.

https://dx.doi.org/10.1021/acscatal.0c04888
ACS Catal. 2021, 11, 3638−3661

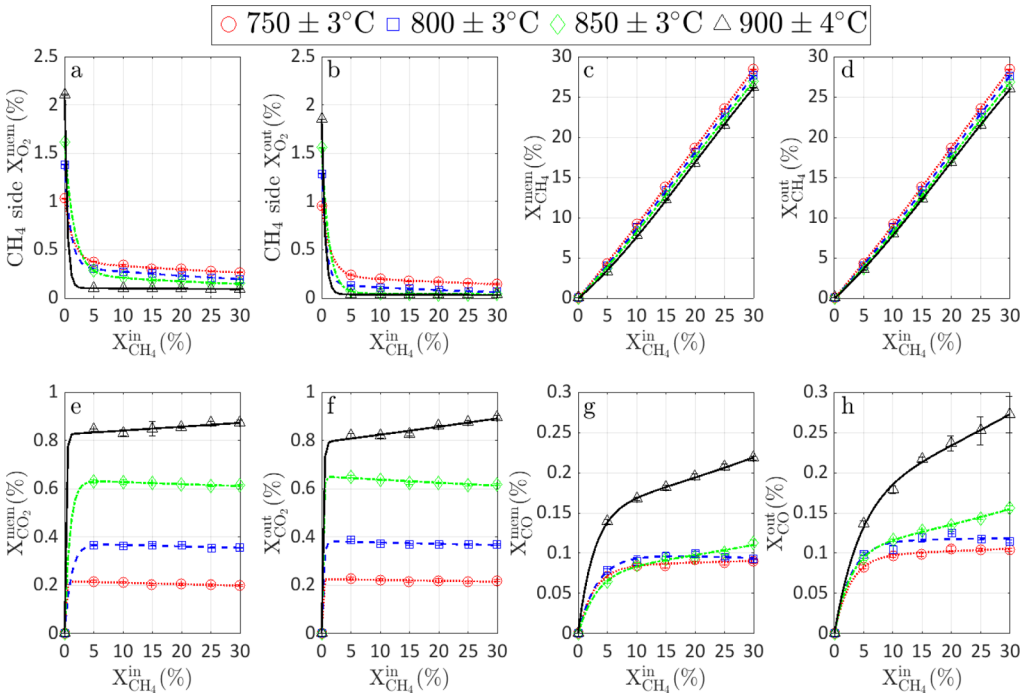

Figure 11. Steady-state species mole fractions near the CH_4 side of the BFZ91 membrane (measured using an alumina micro-probe) and at the outlet as a function of T and $X^{in}_{CH_4}$. (a) CH_4 side $X^{mem}_{O_2}$, (b) CH_4 side $X^{out}_{O_2}$, (c) $X^{mem}_{CH_4}$, (d) $X^{out}_{CH_4}$, (e) $X^{mem}_{CO_2}$, (f) $X^{out}_{CO_2}$, (g) X^{mem}_{CO}, and (h) X^{out}_{CO}. Color marker-line equivalence: (1) $T = 750 \pm 3$ °C: red circles-dotted line, (2) $T = 800 \pm 3$ °C: blue squares-dashed line, (3) $T = 850 \pm 3$ °C: green diamonds-dashed dotted line, and (4) $T = 900 \pm 4$ °C: black triangles-solid line. Lines are guides to the eye. The thickness of the membrane was 0.68 mm, while the thickness of the La_2O_3 catalyst layer was 1.5 mm.

which clearly demonstrate the high stability of BFZ91 and La_2O_3 towards C_2 production. During the entire 23-day experiment, J_{O_2} and $\tilde{n}^{out}_{C_2}$ were stable without any loss of performance. To the best of our knowledge, this is the first time that such long-term OCM measurements are demonstrated with stable membrane-catalyst materials that have been subjected to temperature and fuel cycling for long times. We note here that at 850 and 900 °C, J_{O_2} shows a gradual increase as a function of time for the same $X^{in}_{CH_4}$ value, while the activities of the C_2 species remain constant. This gradual J_{O_2} increase results from the progressive increase of $X^{out}_{CO_2}$ and $X^{out}_{H_2O}$ as a function of time.

Figure 7 shows the XRD patterns of the unused and used BFZ91 and La_2O_3. According to Figure 7, no phase transformations or secondary phases were detected on the air and CH_4 side of the BFZ91 membrane after the end of the OCM measurements. The same is true for the used La_2O_3 powder. For La_2O_3, we have already discussed that we cannot draw a safe conclusion about the formation of stable lanthanum hydroxides and carbonates during OCM based on ex situ XRD; however, recent in operando Raman spectroscopy studies demonstrated the high stability of La_2O_3 under industrially relevant OCM conditions.[62] Nevertheless, the fact that ex situ XRD reveals the absence of secondary phases on La_2O_3 is consistent with the Ellingham diagrams of Figure 4 and the mole fractions of H_2O and CO_2 formed near the membrane surface (Figures 11 and 12 discussed later in Section 3.6). Although the aforementioned results may confirm the high structural stability of the BFZ91 membrane in a hydrocarbon environment and its compatibility with La_2O_3, they do not account for the possible formation of amorphous phases on the membrane or the La_2O_3 catalyst. Such amorphous phases, if present, could degrade the performance under longer trials. Indeed, Schucker et al. have proposed that amorphous phases of $SrCO_3$, SrO, and SrO_2 may exist on Sr-doped La_2O_3 under OCM conditions.[62] In that work, the authors confirm that such amorphous phases cannot be detected by XRD or Raman spectroscopy. However, the study of Schucker et al. does not provide long-term measurements to verify a performance loss as a function of time that could be ascribed to the aforementioned phases.[62] In our work, considering that our 23-day measurement is by itself a long-term trial allows us to conclude that amorphous phases, if present on the materials, do not degrade the OCM performance.

Figure 8 presents the microstructure of the BFZ91 pellet and La_2O_3 powder before and after the OCM measurements. The as-sintered BFZ91 pellet (Figure 8a) shows a large distribution of grain boundary sizes, which range between 0.5−5 μm. No signs of porosity are observed, which confirm the high relative density of the pellet estimated using the Archimedes principle. Figure 8b shows one of the sides of the BFZ91 pellet after polishing. A flat surface is observed with some lines that correspond to scratches from the polishing procedure. Some material expulsion is also noticed despite the fact that a high grit number sandpaper was used to ensure a polished finish. Figure 8c,d shows the air and CH_4 side of the BFZ91 pellet, respectively, after the end of the OCM measurements with La_2O_3. On both sides, surface terraces have become visible within some of the grains, which is probably related to the grain crystallographic orientation and the polishing process as no such terraces are observed in Figure 8a. Similar observations have been reported for other materials[87,88] but the examination of this effect is outside the scope of this work. No particle-like structures are found on either side of the BFZ91 pellet, consistent with the XRD results of Figure 7. The microstructure of the BFZ91 pellet after the end of

https://dx.doi.org/10.1021/acscatal.0c04888
ACS Catal. 2021, 11, 3638−3661

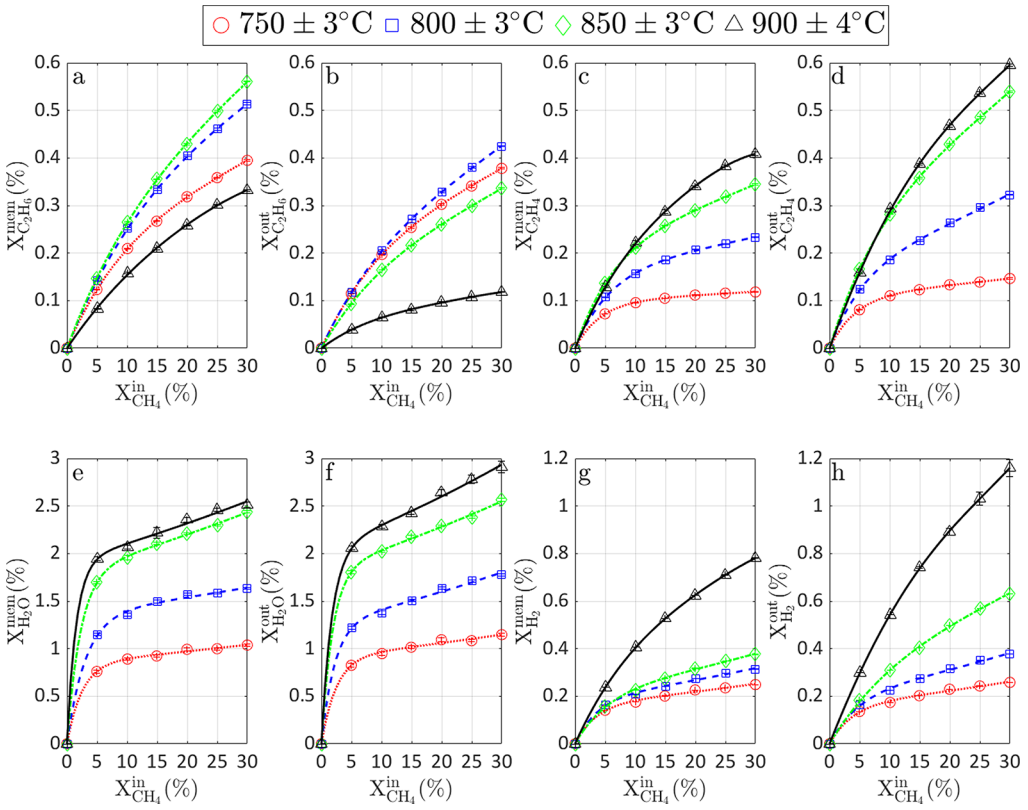

Figure 12. Steady-state species mole fractions near the CH_4 side of the BFZ91 membrane (measured using an alumina microprobe) and at the outlet as a function of T and $X^{in}_{CH_4}$. (a) $X^{mem}_{C_2H_6}$, (b) $X^{out}_{C_2H_6}$, (c) $X^{mem}_{C_2H_4}$, (d) $X^{out}_{C_2H_4}$, (e) $X^{mem}_{H_2O}$, (f) $X^{out}_{H_2O}$, (g) $X^{mem}_{H_2}$, and (h) $X^{out}_{H_2}$. Color marker-line equivalence: (1) $T = 750 \pm 3$ °C: red circles-dotted line, (2) $T = 800 \pm 3$ °C: blue squares-dashed line, (3) $T = 850 \pm 3$ °C: green diamonds-dashed dotted line, and (4) $T = 900 \pm 4$ °C: black triangles-solid line. Lines are guides to the eye. The thickness of the membrane was 0.68 mm, while the thickness of the La_2O_3 catalyst layer was 1.5 mm.

the measurements without La_2O_3 is similar to the one shown in Figure 8c,d. Finally, Figure 8e,f presents the as-purchased and used La_2O_3 powder, respectively. The used powder shows significant sintering because of the high T operation. As shown in Supporting Information Figure S7 comparing the La_2O_3 catalyst after the end of the OCM measurements and after calcination of a fresh catalyst at T = 1025 °C for 24 h, the sintering of the La_2O_3 powder observed, as shown in Figure 8f, is primarily related to the sealing procedure followed in this work and not because of operation in a reactive environment. This also confirms that the sintering of the La_2O_3 catalyst happened before the beginning of the OCM measurements. If this step could be avoided, then, the sintering of the La_2O_3 powder would be lower given that the maximum T investigated in our work is 900 °C. Unfortunately, the amount of the La_2O_3 catalyst used in the OCM experiment is low and did not allow quantification of its surface area using BET.

Finally, based on the XRD and SEM results, as shown in Figures 7 and 8, no signs of carbon deposition are observed on the used materials. In addition, if carbon forms in the products, the presence of H_2O and CO_2 in the mixture at mole fractions between 0.5−2.5 and 0.2−0.9%, respectively (as shown in Figures 11 and 12), would have led to its conversion to H_2 and CO given that the steam gasification of carbon to syngas and the reverse Boudouard are thermodynamically favorable under the conditions investigated in our measurements (T > 700 °C).

3.5. Analysis of BFZ91 and La_2O_3 Steady-State OCM Measurements. At each T and $X^{in}_{CH_4}$, as shown in Figure 6, detailed measurements were obtained after steady state was achieved to shed light into the performance and OCM chemistry. Figures 9-12 present these results.

Figure 9a shows J_{O_2} as a function of T and $X^{in}_{CH_4}$. At T = 750 °C, J_{O_2} is constant at ~0.5 μmol/cm^2/s and independent of $X^{in}_{CH_4}$. However, as T increases, J_{O_2} rises as a function of $X^{in}_{CH_4}$. As discussed earlier, this is related to the rate-limiting steps of the O_2 permeation process. Surface reactions on the CH_4 side are rate limiting at T ≤ 800 °C (in addition to bulk diffusion), and they are accelerated at T ≥ 850 °C. The J_{O_2} increase as a function of $X^{in}_{CH_4}$ at T = 850−900 °C, as shown in Figure 9a, suggests that a low P_{O_2} is developed in the presence of La_2O_3 when CH_4 is added. This will be confirmed in the next section.

In addition to the above, we also make a note about the nonreactive J_{O_2} measurements ($X^{in}_{CH_4}$ = 0%) at 800−900 °C, as shown in Figure 9a. At this temperature range, comparing with Figure 5a reveals that J_{O_2} has decreased slightly in the presence of La_2O_3. Given that the thickness of the BFZ91 membrane was almost the same for both experiments, we suspect that the slight decrease in the nonreactive J_{O_2} could be related to the presence of the La_2O_3 powder on the CH_4 side of the membrane. La_2O_3 could restrict gaseous diffusion through its porous structure thus decreasing J_{O_2}. In any case, the performance drop observed in our measurements was not remarkable, and hence, if the slight drop in J_{O_2} is not related to experimental uncertainties but is

https://dx.doi.org/10.1021/acscatal.0c04888
ACS Catal. 2021, 11, 3638−3661

because of the presence of La_2O_3, we conclude that the latter does not significantly impact J_{O_2}, especially when CH_4 is added in the reactor.

Figure 9b shows C_{CH_4} as a function of T and $X^{in}_{CH_4}$. Higher C_{CH_4} is achieved as T increases given the Arrhenius activated behavior of gas phase and surface (membrane and catalyst) reactions. At the same T, adding more fuel decreases C_{CH_4} showing that less fraction of CH_4 can be converted to the products. Figure 9c,d shows $S_{C_2H_6}$ and $S_{C_2H_4}$, respectively. The system is less selective to the formation of C_2H_6 as T increases. The trend is opposite for C_2H_4, whose selectivity increases as a function of T except at 900 °C. At the same T, adding more CH_4 increases the selectivity with the exception of $S_{C_2H_6}$ at 900 °C and of $S_{C_2H_4}$ at 750 °C, where nearly constant values are observed. These trends can be explained by the conversion of C_2H_6 to C_2H_4, which, in general, can happen in the gas phase and on the La_2O_3 catalyst through oxidative and non-oxidative pathways.

To obtain further insights about the aforementioned reactions, we examined the NODHE in the absence and presence of La_2O_3 between T = 750−900 °C; this experiment is described in the Supporting Information (Section 7). Supporting Information Figure S9 shows that at equilibrium, C_2H_6 is fully converted to products even at T = 750 °C. The mole fraction of C_2H_4 is finite but low and the system favors the production of CH_4, H_2, and C_2H_2. Under non-equilibrium conditions, Supporting Information Figure S9 shows identical C_2H_6 thermal decomposition with and without La_2O_3. As a result, we can safely conclude that La_2O_3 is not active toward the C_2H_6 and C_2H_4 non-oxidative dehydrogenation, which can only happen in the gas phase. Supporting Information Figure S9 reveals that the conversion of C_2H_6 at T = 750 °C approaches ≈80%, while full conversion to products is achieved at T = 850 °C. Most of C_2H_6 is converted to C_2H_4 and H_2 with C_2H_2 and CH_4 also being present but at lower mole fractions. The produced C_2H_4 peaks at T ≈ 780 °C, and then, it decreases because of decomposition to C_2H_2, CH_4, and H_2. These results confirm the presence of both C_2H_6 and C_2H_4 non-oxidative dehydrogenation in the gas-phase, which depend on the residence time and become more intense as the temperature rises. Hence, we demonstrate that one pathway for C_2H_4 production is the NODHE in the gas phase; this reaction does not proceed on La_2O_3. The possibility of the oxidative dehydrogenation of C_2H_6 (ODHE) to C_2H_4 and H_2O (either in the gas phase or on La_2O_3) will be discussed in the next section.

The yields (Figure 9e,f) and activities (Figure 9g,h) of C_2H_6 and C_2H_4 show similar trends. For the same $X^{in}_{CH_4}$, $Y_{C_2H_6}$ and $\tilde{n}_{C_2H_6}$ increase at 800 °C compared to 750 °C, but a sharp drop is observed at 850 °C and 900 °C because of C_2H_6 conversion to C_2H_4. In contrast, $Y_{C_2H_4}$ and $\tilde{n}_{C_2H_4}$ clearly increase as T rises. However, the increase at 900 °C compared to the 850 °C case is small, confirming that C_2H_4 either pyrolyzes at high T similar to C_2H_6 (see Supporting Information Figure S9) or reacts with other products. At the same T, $Y_{C_2H_6}$ and $Y_{C_2H_4}$ drop as a function of $X^{in}_{CH_4}$, a sign that the formation of the desired products is limited by the insufficient amount of O_2 through the membrane that has already been fully converted to products (C_{O_2} ≈ 100%, see Figure 11b). However, at the same T, both $\tilde{n}_{C_2H_6}$ and $\tilde{n}_{C_2H_4}$ increase as more fuel is introduced in the CH_4 side, which is consistent with the known trend of higher C_2 selectivity under fuel-rich conditions.

Figure 10 shows the selectivities and yields of the rest of the species produced within the reactor. Figure 10a−d demonstrates that the La_2O_3 catalyst is selective toward the formation of H_2O and CO_2 with yields higher than those of C_2H_6 and C_2H_4. This suggests that, in addition to CH_4 coupling to C_2, hydrocarbon full oxidation to H_2O and CO_2 also takes place. For both H_2O and CO_2 and at the same $X^{in}_{CH_4}$, Figure 10a−d shows that between T = 750−900 °C, the selectivity and yield increase as T rises because of the Arrhenius-activated nature of the reactions. However, at the same T, addition of more CH_4 in the reactor decreases S_{H_2O} and S_{CO_2}. Comparison with Figure 9c,d confirms that the system becomes more selective toward the formation of C_2 by adding more fuel in the reactor. As discussed earlier, this is consistent with the literature suggesting that increased C_2 selectivities can be achieved at high CH_4 to O_2 ratios.[12,26]

At T = 750−850 °C, Figure 10e−h shows that the selectivities to H_2 and CO are below 15%, while the corresponding yields are lower than 2%. This confirms that the system is not very active toward syngas production. However, a different trend is observed at 900 °C. At this T, an increase in the yields of H_2 and CO is observed. As will be discussed in the next section, this behavior is related to several competing reactions leading to syngas production because of enhanced gas-phase reactivity at 900 °C.

3.6. Mixture Composition near the CH_4 Side Gas−Membrane Interface and Comparison with Outlet Values. In Section 3.5, we analyzed the steady-state performance of BFZ91 with La_2O_3 toward CH_4 conversion to products. Based on Figures 9, 10, and Supporting Information Figure S9, significant information was obtained about the primary reactions of the OCM chemistry with and without La_2O_3. However, Figures 9 and 10 focus on measurements at the outlet of the reactor. It has already been demonstrated in Section 3.3 that measurements at the outlet can be different compared to measurements near the membrane surface. This is true when the mixture composition includes species with significant gas-phase reactivity (such as CH_4, C_2H_6 and C_2H_4) and becomes more important as T rises. In the presence of La_2O_3, measurements with an alumina micro-probe near the membrane surface allow us to identify the reactions taking place due to the membrane-catalyst interaction. At the same time, these measurements provide information about gas-phase reactions not related to the membrane-catalyst presence such as the ones happening in the reactor's post-catalytic zone. Figures 11 and 12 compare the CH_4 side membrane (i.e., near the membrane surface but still in the gas-phase and within the La_2O_3 bed) and outlet (i.e. at the outlet of the reactor) mole fractions of O_2, CH_4, CO_2, CO, C_2H_6, C_2H_4, H_2O, and H_2. For the entire data set, mole fractions less than 0.01% were measured for propane, propene, propadiene, and propyne. C_2H_2 was zero at 750−850 °C, while mole fractions between 0.01 and 0.05% were measured at 900 °C.

In the absence of fuel (i.e., for the cases with $X^{in}_{CH_4}$ = 0%), Figure 11a shows that $X^{mem}_{O_2}$ increases as T rises, consistent with the higher J_{O_2} observed in Figure 9a. When CH_4 is added, the presence of the catalyst reduces $X^{mem}_{O_2}$ significantly and leads to conditions where C_{O_2} ≈ 100% (Figure 11b). At T = 750−800

https://dx.doi.org/10.1021/acscatal.0c04888
ACS Catal. 2021, 11, 3638−3661

°C, surface reactions at the CH_4 side limit J_{O_2}, and hence, J_{O_2} is almost constant despite the fact that a low P_{O_2} environment evolves in the vicinity of the membrane. At higher T, surface reactions are accelerated, and hence, J_{O_2} increases at T = 850−900 °C as more CH_4 is added. Figure 11b shows that $X_{O_2}^{out}$ follows the same trend as $X_{O_2}^{mem}$, with $X_{O_2}^{mem} > X_{O_2}^{out}$ for all experimental points. For nonreactive cases, the trend is consistent given that a higher mole fraction of O_2 is expected near the membrane surface, which then decreases at the outlet because of gaseous diffusion. For reactive cases, the results demonstrate that most of the reaction of O_2 with CH_4 (or other products) takes place near the OCM catalyst with the remaining O_2 reacting in the gas phase with CH_4 or other products as the mixture exits the reactor.

Figure 11c,d shows that a significant fraction of CH_4 remains nonreactive both near the membrane surface and at the outlet, consistent with the relatively low C_{CH_4}, as reported in Figure 9b. However, mole fractions at the outlet are lower than the ones near the membrane; the trend is more apparent as the temperature increases and is consistent with gas-phase reactivity as the mixture exits the reactor. For the same $X_{CH_4}^{in}$, less CH_4 is measured at higher T, which explains the higher C_{CH_4} observed as T rises.

Figures 11e and 12e show that significant quantities of CO_2 and H_2O form within the La_2O_3 catalyst. The fact that $X_{H_2O}^{mem}/X_{CO_2}^{mem} > 2$ suggests the full oxidation of CH_4. The full oxidation of C_2H_6 and C_2H_4 to CO_2 and H_2O results in X_{H_2O}/X_{CO_2} equal to 1.5 and 1, respectively. Clear evidence of CH_4 full oxidation is also shown in Supporting Information Figure S12a (partial O_2 consumption experiment discussed in section 3.7). At T = 750−850 °C, the mole fractions of CO_2 and H_2O near the membrane surface are nearly the same as the ones at the outlet (see Figures 11f and 12f). This demonstrates that CH_4 full oxidation takes place within the La_2O_3 bed, and then, the produced H_2O and CO_2 transport to the exit of the reactor without reacting much with CH_4 or with other products. In addition, Figure 12a,c shows that both C_2H_6 and C_2H_4 form near the membrane surface and within the La_2O_3 bed. This observation coupled with the fact that $X_{H_2O}^{mem}/X_{CO_2}^{mem} > 2$ suggests that CH_4 full oxidation to CO_2 and H_2O is happening simultaneously with CH_4 oxidative coupling to C_2H_6 and H_2O (reaction 1). Both are facilitated by the presence of the La_2O_3 catalyst as the aforementioned reactions are not observed at considerable rates in the absence of La_2O_3 (Figure 5). C_2H_6 is known to precede the formation of C_2H_4; this is verified by the aforementioned results and has also been confirmed by others.[89,90]

Next, we attempt to identify the pathway of the C_2H_4 formation from C_2H_6. To do so, we consider the results, as shown in Figures 11 and 12. These plots confirm the existence of the following primary species within the La_2O_3 catalyst: H_2O, CO_2, C_2H_6, C_2H_4, H_2, CO, and unreacted CH_4. We note that because O_2 is fully consumed near the membrane, the formation of C_2H_4 and H_2 through NODHE takes place in the oxygen-free zone between the La_2O_3 catalyst and the exit of the reactor (compare Figure 12a with Figure 12b etc.). This is known from our previous work and that of others.[57,58,91] To remove the effect of this reaction from the analysis of the reactions happening on La_2O_3, we will focus on the measurements near the membrane surface and within the La_2O_3 catalyst (i.e., we do not consider the outlet data). By looking at Figure 12c,g, we observe that for a fixed T, $X_{C_2H_4}^{mem}$ and $X_{H_2}^{mem}$ increase as $X_{CH_4}^{in}$ increases. Based on this observation, the production of C_2H_4 and H_2 can be the result of the following pathways:

- Pathway 1: ODHE to C_2H_4 and H_2O followed by reaction to syngas. This pathway can be described through the following global reactions:

$$C_2H_6 + \frac{1}{2}O_2 \rightarrow C_2H_4 + H_2O \tag{11}$$

$$C_xH_y + \frac{x}{a-c}O_aH_bC_c \rightarrow \frac{ax}{a-c}CO + \left(\frac{y}{2} + \frac{bx}{2(a-c)}\right)H_2 \quad a \neq c \tag{12}$$

Regarding syngas production (reaction 12), we note that in general, syngas can be produced through oxidation, steam- or dry-reforming of CH_4, C_2H_6 and C_2H_4. In this analysis, we are interested in the fact that syngas is produced through any reaction after ODHE. Hence, we can consider only one of these reactions without the loss of generality.

If this is the pathway taking place on La_2O_3, then, at a fixed T, both X_{CO}^{mem} and $X_{H_2}^{mem}$ should increase as $X_{CH_4}^{in}$ increases. At T = 750−850 °C, Figure 11g reveals an almost constant X_{CO}^{mem} at $X_{CO}^{mem} \approx 0.10\%$, while Figure 12g clearly shows that $X_{H_2}^{mem}$ is increasing. The constant X_{CO}^{mem} confirms that this pathway is not taking place at high rates. The production of H_2 should be accompanied by the production of CO if syngas production is taking place on La_2O_3 after ODHE. The constant value of X_{CO}^{mem} also rules out the possibility of H_2 being produced through the water gas shift (WGS) as this would lead to decrease in X_{CO}^{mem}.

- Pathway 2: NODHE to C_2H_4 and H_2. This pathway can be described through the following reaction:

$$C_2H_6 \rightarrow C_2H_4 + H_2 \tag{13}$$

At T = 750−850 °C, Figure 12c,g shows that $X_{C_2H_4}^{mem} \approx X_{H_2}^{mem}$ but $X_{H_2}^{mem}$ is always slightly higher than $X_{C_2H_4}^{mem}$. In conjunction with the fact that X_{CO}^{mem} is nearly constant at $X_{CO}^{mem} \approx 0.10\%$, this confirms the validity of this pathway. We have already shown that NODHE does not happen on La_2O_3 (Supporting Information Figure S9). The produced H_2 of this pathway has 2 contributions: (a) from one or multiple reactions producing syngas, which, however, are slow and kinetically frozen at T = 750−850 °C after some CO and H_2 have been produced at low $X_{CH_4}^{in}$ and (b) from NODHE.

The aforementioned analysis confirms that ODHE is not a major reaction within our membrane reactor. However, this does not mean that the reaction does not happen at all on La_2O_3 but rather, that within our reactor, the rate of ODHE on La_2O_3 is smaller than the rate of the primary reaction, NODHE (in the gas phase). However, evidence of ODHE has been reported in the literature, although the investigated catalysts were not pure La_2O_3 as in our study. For example, Stansch et al.[91] proposed ODHE to proceed on La-impregnated CaO, and they also added ODHE in their proposed reaction mechanism. However, SEM images were not provided in that work to identify whether the impregnation results to discrete La_2O_3 particles on CaO or to a full coating of CaO with La_2O_3. If the former is true, then a question that arises is whether the ODHE takes place on La_2O_3

https://dx.doi.org/10.1021/acscatal.0c04888
ACS Catal. 2021, 11, 3638−3661

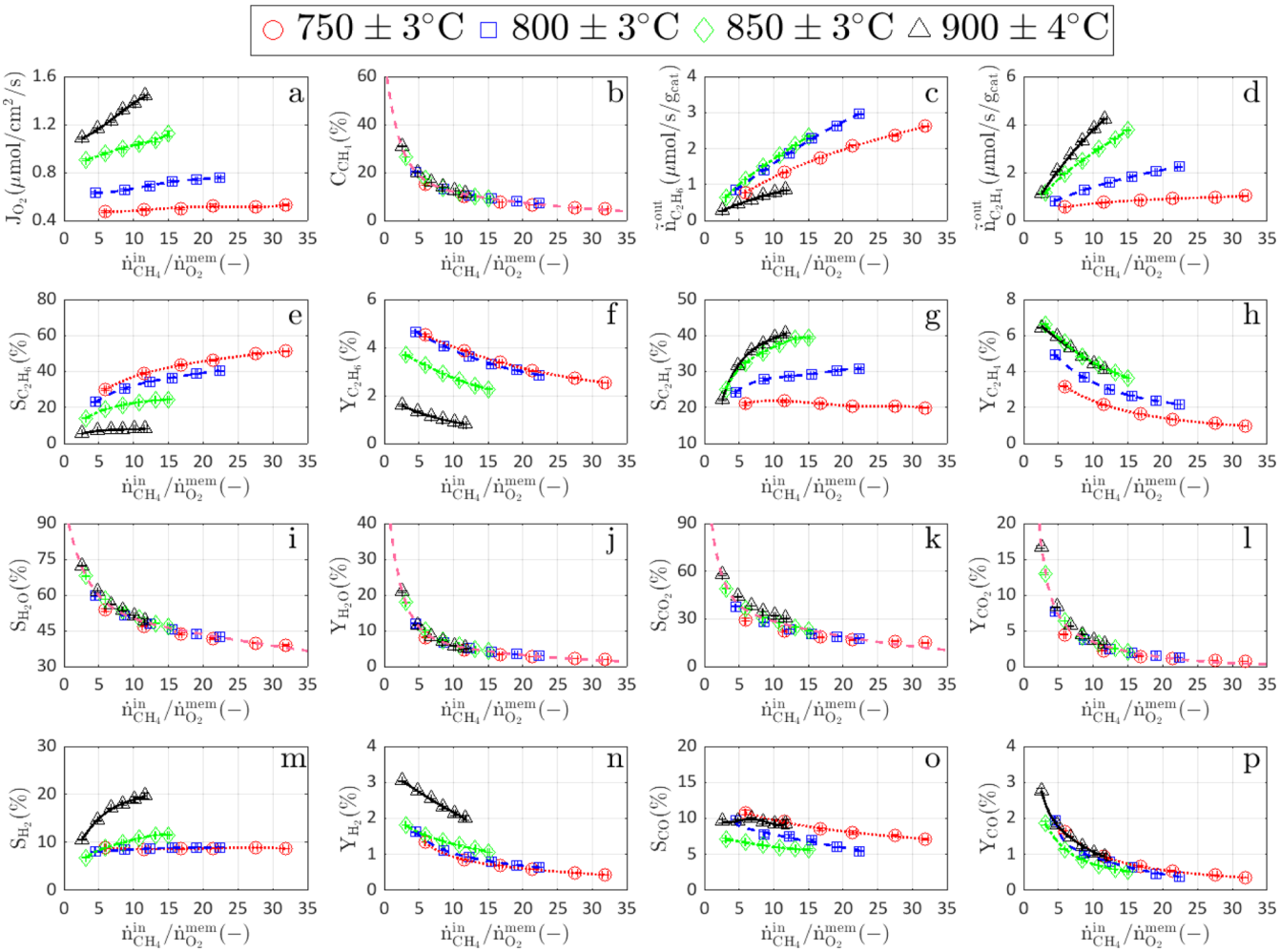

Figure 13. Selected performance metrics as a function of T and $\dot{n}^{in}_{CH_4}/\dot{n}^{mem}_{O_2}$: (a) J_{O_2}, (b) C_{CH_4} ($y = 51.01e^{-0.491x} + 18.13e^{-0.04458x}$, $R^2 = 0.9921$), (c) $\tilde{\dot{n}}^{out}_{C_2H_6}$, d) $\tilde{\dot{n}}^{out}_{C_2H_4}$, (e) $S_{C_2H_6}$, (f) $Y_{C_2H_6}$, (g) $S_{C_2H_4}$, (h) $Y_{C_2H_4}$, (i) S_{H_2O} ($y = 43.95e^{-0.3387x} + 54.71e^{-0.01155x}$, $R^2 = 0.9797$), (j) Y_{H_2O} ($y = 46.16e^{-0.5083x} + 9.798e^{-0.05599x}$, $R^2 = 0.9932$), (k) S_{CO_2} ($y = 90.35e^{-0.6219x} + 42.36e^{-0.04034x}$, $R^2 = 0.9279$), (l) Y_{CO_2} ($y = 65.08e^{-0.7467x} + 9.065e^{-0.09846x}$, $R^2 = 0.9859$), (m) S_{H2}, (n) Y_{H_2}, (o) S_{CO}, and (p) Y_{CO}. Color marker-line equivalence: (1) $T = 750 \pm 3$ °C: red circles-dotted line, (2) $T = 800 \pm 3$ °C: blue squares-dashed line, (3) $T = 850 \pm 3$ °C: green diamonds-dashed dotted line, and (4) $T = 900 \pm 4$ °C: black triangles-solid line. When the data collapse on the same curve, the curve is plotted using a pink dashed line; see the caption of each subplot for the corresponding equation and the goodness of fit.

or CaO or at their interface. In a similar way, Choudhary et al.[92] investigated ODHE over a Sr- and La-impregnated SA5205 support (consisting primarily of Al_2O_3 with some SiO_2). Although this paper confirms the presence of the ODHE reaction, it does not provide any data or conclusions in terms of whether this reaction proceeds in the gas phase or on the surface of the catalyst (on SrO or on La_2O_3 or at the SrO−La_2O_3 interface) or both. SEM images were not provided to investigate the catalyst's microstructure. In addition, the catalyst support was considered to be inert but results validating this hypothesis were not provided. Hence, given the different materials and the unknown microstructure of these catalysts compared to pure La_2O_3 as well as the lack of key evidence, we conclude that the work by Stansch et al.[91] and Choudhary et al.[92] do not clearly support an ODHE pathway over pure La_2O_3.

The discussion above focuses on measurements between T = 750−850 °C, for which, the low and constant values of X^{mem}_{CO} suggest that syngas reactions in the vicinity of La_2O_3 are slow and kinetically frozen, respectively. At T = 900 °C, our results show that reactions producing syngas are not kinetically frozen anymore and that gas-phase reactions are accelerated significantly. This is true even in the absence of La_2O_3 (see Figure 5). At T = 900 °C, there are several competing reactions leading to syngas production that should be considered, which complicates the analysis. First, under the operating T of this study, it is known that CH_4, C_2H_6, and C_2H_4 can be partially oxidized or reformed (with H_2O and/or CO_2) into syngas.[26,91] Second, the formation of CO and H_2O through the reverse WGS reaction is favored thermodynamically at T > 818 °C, while the formation of CO_2 and H_2 is favored at lower T. Third, decomposition of C_2H_4 is also accelerated as T increases. For example, at T = 900 °C, $X^{mem}_{H_2} \gg X^{mem}_{C_2H_4}$ and we attribute this to the additional non-oxidative dehydrogenation of C_2H_4 in the gas phase. Therefore, although our proposed mechanism is clear for T = 750−850 °C given that the aforementioned reactions are sluggish within this temperature regime, the multiple competing pathways because of the enhanced gas-phase chemistry at T = 900 °C make the analysis at this T difficult. At this T, a safe conclusion about the reactions leading to syngas production is only possible through the use of computational models, and hence, no further analysis

https://dx.doi.org/10.1021/acscatal.0c04888
ACS Catal. 2021, 11, 3638−3661

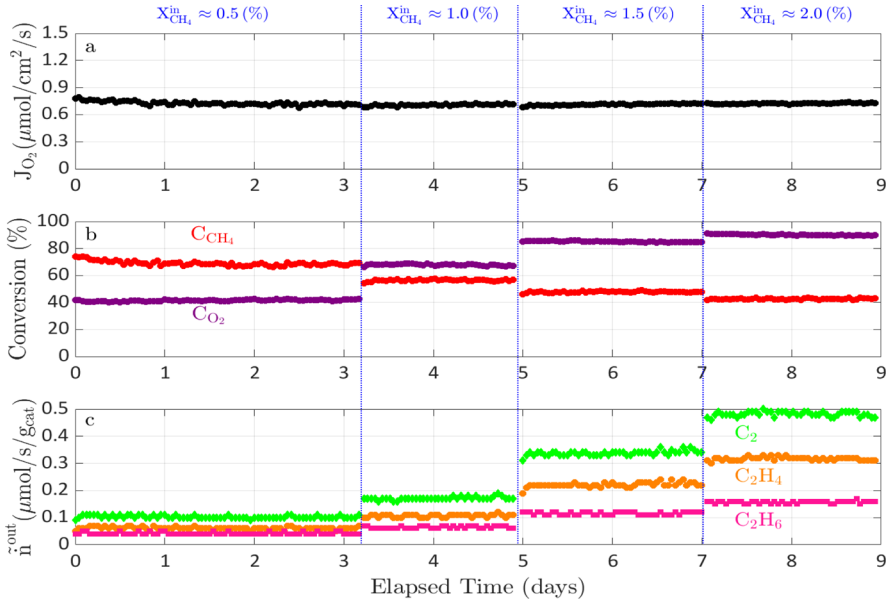

Figure 14. Long-term performance of BFZ91 with La_2O_3 at T = 850 °C under partial O_2 consumption conditions. (a) J_{O_2} (black) as a function of time and $X^{in}_{CH_4}$, (b) C_{CH_4} (red) and C_{O_2} (purple) as a function of time and $X^{in}_{CH_4}$, and (c) $\tilde{n}^{out}_{C_2H_6}$ (pink), $\tilde{n}^{out}_{C_2H_4}$ (orange), and $\tilde{n}^{out}_{C_2}$ (green) as a function of time and $X^{in}_{CH_4}$. Blue dotted lines correspond to instants of $X^{in}_{CH_4}$ change. Measurements were conducted every 1 h. During the experiment, ambient air was flowing in the air side at $\dot{Q}_{air}$ = 200 sccm, while CH_4−Ar mixtures with $\dot{Q}^{total}_{CH_4-Ar}$ = 100 sccm were introduced in the CH_4 side. The thickness of the membrane was 0.66 mm, while the thickness of the La_2O_3 catalyst layer was 1.5 mm.

on the reactions resulting to syngas production will be attempted here.

To enable the comparison of the results of this work with other studies in the literature, we decided to plot the most important performance metrics as a function of T and $\dot{n}^{in}_{CH_4}/\dot{n}^{mem}_{O_2}$, that is, the ratio of the CH_4 mole flow rate at the inlet of the CH_4 side over the mole flow rate of O_2 through the membrane. This definition is consistent with the standard used in traditional OCM, where results are plotted as a function of T and X_{CH_4}/X_{O_2} given that CH_4 and O_2 are co-fed at the inlet of the reactor. Figure 13 summarizes the results and reveals some very interesting trends. First, although the independent variables of our measurements are T and $X^{in}_{CH_4}$, we observe that $\dot{n}^{in}_{CH_4}/\dot{n}^{mem}_{O_2}$ is not constant at each T. Given that J_{O_2} increases at higher T and as more CH_4 is introduced in the reactor, the operating window of $\dot{n}^{in}_{CH_4}/\dot{n}^{mem}_{O_2}$ narrows down. Second, the results reveal that the highest C_2H_6 and C_2H_4 yields are obtained as $\dot{n}^{in}_{CH_4}/\dot{n}^{mem}_{O_2}$ decreases while the highest selectivities are obtained as $\dot{n}^{in}_{CH_4}/\dot{n}^{mem}_{O_2}$ increases. The highest C_2 yield is $Y_{C_2} \approx 10.3\%$ obtained at T = 850 °C for $\dot{n}^{in}_{CH_4}/\dot{n}^{mem}_{O_2} \approx 3.1$, which is very close to a stoichiometric ratio of 2. Finally, we observe that for some of the performance metrics (C_{CH_4}, S_{H_2O}, Y_{H_2O}, S_{CO_2}, and Y_{CO_2}), all data points collapse into the same curve demonstrating that they depend exclusively on $\dot{n}^{in}_{CH_4}/\dot{n}^{mem}_{O_2}$ (recall, though, that $\dot{n}^{mem}_{O_2}$ is a function of T and $\dot{n}^{in}_{CH_4}$); however, this is not the case for the species of interest, that is, $S_{C_2H_6}$, $Y_{C_2H_6}$, $S_{C_2H_4}$, and $Y_{C_2H_4}$ although some similarity is observed for a part of the data (e.g., for $Y_{C_2H_6}$ at T = 750−800 °C and for $Y_{C_2H_4}$ at T = 850−900 °C). Based on the activation barriers (E_a) reported by Stansch et al.,[91] E_a = 48 − 68 (kJ/mol) for CH_4 oxidation (partial and full) while E_a = 168 − 182 (kJ/mol) for C_2H_6 and C_2H_4 formation. Such high E_a values do not support the observed temperature independence for some performance metrics given that $E_a/RT \approx 5-18$. They do explain, however, the temperature dependency for C_2. Because the C_2H_6 and C_2H_4 non-oxidative dehydrogenation happens in the gas phase within oxygen-free zones, the residence time is another variable that affects the aforementioned trends for C_2. However, further studies are required to elucidate the reasons why an explicit temperature independence is observed for C_{CH_4}, S_{H_2O}, Y_{H_2O}, S_{CO_2}, and Y_{CO_2}. To the best of our knowledge, this is the first time that such similarity curves are reported for OCM and can be very useful as first-order estimates when designing commercial-scale reactors.

3.7. Performance and Stability of BFZ91 and La_2O_3 under Partial O_2 Consumption and under an Undiluted CH_4 Stream. In the previous sections, we demonstrated the stability of BFZ91 with La_2O_3 under conditions of full O_2 consumption (Figure 11a,b). However, Hayek et al. have reported that OCM catalysts may still undergo deactivation, which is masked if operating at $C_{O_2} \approx 100\%$; they confirmed this behavior for the Mn_xO_y−Na_2WO_4/SiO_2 catalyst.[93] Although this catalyst is known to be very unstable and to exhibit different phase transformations leading to OCM performance loss as a function of time,[94] we decided to conduct another stability test, this time under conditions of partial O_2 consumption. The experiment was conducted using a new BFZ91 pellet and fresh La_2O_3 powder. Given that J_{O_2} is a function of T, $X^{in}_{CH_4}$ and membrane thickness, we fixed the temperature at T = 850 °C, and the membrane thickness at 0.66 mm while varying $X^{in}_{CH_4}$. To cover more than one values of C_{O_2}, we conducted long-term measurements at different $X^{in}_{CH_4}$.

https://dx.doi.org/10.1021/acscatal.0c04888
ACS Catal. 2021, 11, 3638−3661

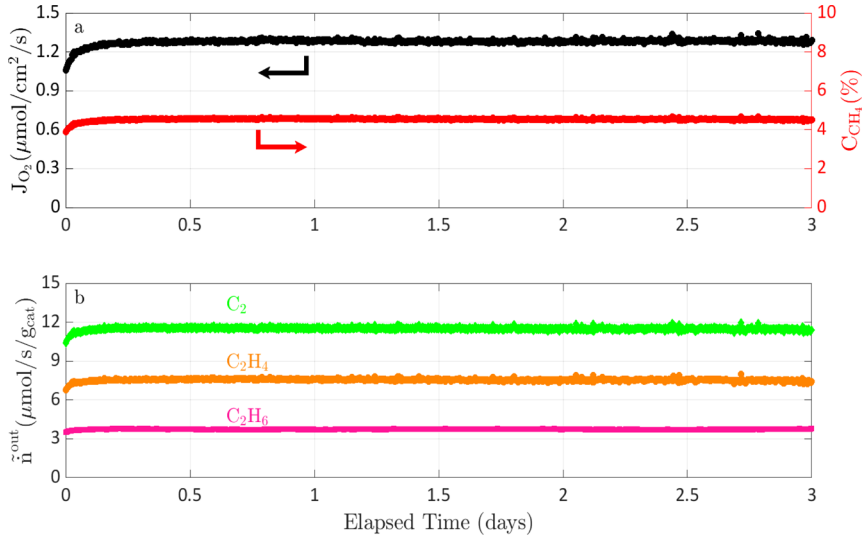

Figure 15. Long-term performance of BFZ91 with La_2O_3 at T = 850 °C under pure CH_4. (a) J_{O_2} (black) and C_{CH_4} (red) as a function of time and (b) $\tilde{n}^{out}_{C_2H_6}$ (pink), $\tilde{n}^{out}_{C_2H_4}$ (orange), and $\tilde{n}^{out}_{C_2}$ (green) as a function of time. Measurements were conducted every 4 min. During the experiment, ambient air was flowing in the air side at $\dot{Q}_{air}$ = 200 sccm while pure CH_4 with $\dot{Q}_{CH_4}$ = 100 sccm was introduced in the CH_4 side. The thickness of the membrane was 0.66 mm, while the thickness of the La_2O_3 catalyst layer was 1.5 mm.

Figure 14 shows J_{O_2}, C_{CH_4}, C_{O_2}, and the activities of C_2H_6, C_2H_4, and C_2 as a function of time and $X^{in}_{CH_4}$. In addition, Supporting Information Figures S10−S12 show the species selectivities, yields, and outlet mole fractions, respectively. The results reveal some equilibration in the first few hours of the experiment after which the performance is very stable as a function of time. For comparison, Hayek et al. reported a significant performance loss within the first 4 days of measurements. In the case of La_2O_3, no deactivation was observed for 9 days of measurements under conditions of partial O_2 consumption.

Having demonstrated the stability of BFZ91 with La_2O_3 in the aforementioned regime, we decided to continue the stability experiment using the same materials, but this time we used pure CH_4 at the CH_4 side. The OCM performance as a function of time is shown in Figure 15 and in Supporting Information Figure S13. The experiment lasted for 3 days after which it was terminated because no degradation was observed. The analysis of the mixture composition at the outlet of the CH_4 side was conducted every 4 min. After an equilibration period that took place within the first few hours of the measurement, J_{O_2}, C_{CH_4}, and the corresponding activities remained stable as a function of time. Under these conditions, C_{O_2} = 100%. J_{O_2} increased significantly because of operation under a reducing environment and reached $J_{O_2} \approx 1.3$ (μmol/cm^2/s). Despite this J_{O_2} increase, $C_{CH_4} \approx 4.5\%$ which is low because of the limited amount of O_2 permeating through a low surface area lab-scale membrane. Operation at T = 850 °C with a 0.66 mm thick BFZ91 membrane under pure CH_4 results to $\dot{n}^{in}_{CH_4}/\dot{n}^{mem}_{O_2} \approx 45$ in our lab-scale reactor, which is significantly higher than ratios of 5−10 expected under industrial-scale OCM conditions. For this reason, high selectivities and low yields of C_2H_6 and C_2H_4 are obtained (see Supporting Information Figure S13).

XRD results of the used materials show the absence of secondary phases (Supporting Information Figure S14). Although the air side BFZ91 and the La_2O_3 catalyst microstructures shown in Supporting Information Figure S15a,c, respectively, do not reveal any differences when compared to the ones, as shown in Figure 8, this is not the case for the CH_4 side BFZ91 surface. As shown in Supporting Information Figure S15b, several particles with different sizes and shapes have evolved on this surface. EDS mapping (Supporting Information Figure S16) confirms that these particles are enriched in Fe but depleted in Ba and Zr, although this depletion is not significant (i.e., Ba and Zr still exist within the Fe-enriched zones); this does not point out to the formation of metallic Fe (Fe^0) or Fe oxides (Fe_xO_y). These results suggest that secondary Fe-enriched $Ba_xFe_yZr_zO_a$ phases formed on the CH_4 side of the BFZ91 membrane and are possibly related to the decomposition of the BFZ91 membrane because of the extremely reducing environment ($\dot{n}^{in}_{CH_4}/\dot{n}^{mem}_{O_2} \approx 45$). These particles do not exist on the CH_4 side of BFZ91 between $X^{in}_{CH_4} = 0 - 30\%$ (Figure 8d). This Fe-enriched $Ba_xFe_yZr_zO_a$ phase is not amorphous (because it is analyzed through SEM−EDS), so a possible reason why it was not observed through XRD is because XRD is a bulk characterization technique, and this phase is probably located primarily on the surface of BFZ91 and not within its bulk.

We do not currently know at which stage of the 3-day experiment with pure CH_4 this Fe-enriched $Ba_xFe_yZr_zO_a$ phase started forming. One hypothesis is that this phase formed progressively as a function of time. If this is the case, then Figure 15 confirms that it did not impact the performance of BFZ91 because no degradation was observed. However, longer trials are required to demonstrate if the performance can be compromised under prolonged exposure to pure CH_4. Another hypothesis is that this phase formed soon after pure CH_4 was introduced in the reactor. This could explain the reason of the observed equilibration within the first few hours of the experiment. If the aforementioned Fe-enriched $Ba_xFe_yZr_zO_a$ phase formed during this stage, it resulted in performance enhancement both in terms of J_{O_2} as well as C_2 production (Figure 15); and some studies have shown that similar perovskite oxides (e.g., $Ba_{0.5}Sr_{0.5}FeO_{3-\delta}$) are active OCM catalysts.[37] The performance

https://dx.doi.org/10.1021/acscatal.0c04888
ACS Catal. 2021, 11, 3638−3661

remained stable for the rest of the measurement, confirming that if this phase forms at the beginning of exposure to CH_4, it does not degrade the performance of BFZ91 with La_2O_3. Further studies are required to fully identify the stoichiometry of the proposed Fe-enriched $Ba_xFe_yZr_zO_a$ phase and whether it is indeed active for OCM. Finally, some carbon deposition is observed on the CH_4 side of the BFZ91 membrane (Supporting Information Figure S16), which is confined to a few discrete locations and does not appear to degrade the performance of the investigated materials.

3.8. OCM Mechanism of BFZ91 with La_2O_3: Global Reactions, Rate-Limiting Steps, and Species Activation on the Catalyst. Based on the results, as shown in Figures 9−12, and the discussion in Sections 3.5−3.7, we have clearly identified the following global reactions on a macroscopic level when using BFZ91 membranes coupled with La_2O_3:

$$\frac{1}{2}O_2(g) + V_O^{\bullet\bullet} + 2Fe'_{Fe} \overset{BFZ91}{\rightleftharpoons} O_O^x + 2Fe^x_{Fe} \quad (14)$$

$$CH_4(g) + 2O_2(g) \xrightarrow{La_2O_3} CO_2(g) + 2H_2O(g) \quad (15)$$

$$2CH_4(g) + \frac{1}{2}O_2(g) \xrightarrow{La_2O_3} C_2H_6(g) + H_2O(g) \quad (16)$$

$$C_2H_6(g) \rightarrow C_2H_4(g) + H_2(g) \quad (17)$$

For reactions 14−17, (g) denotes a species in the gas phase. Reaction 14 is written assuming that electrons are the main charge carriers for electronic conductivity, which is consistent with the defect chemistry of $BaFe_{0.95}Zr_{0.05}O_{3-\delta}$.[68] Although the determination of the exact defect chemistry of BFZ91 is outside the scope of this work and will be addressed in future publications, it is reasonable to conclude that the defect chemistry between BFZ91 and $BaFe_{0.95}Zr_{0.05}O_{3-\delta}$ will be similar. The forward step of reaction 14 takes place on the air side gas-membrane interface and incorporates O_2 into the membrane; the reverse reaction occurs on the CH_4 side interface and releases O_2 into the gas phase. As discussed earlier, we have excluded the possibility of the CH_4 reaction with O_O^x on the gas−membrane interface or with O_2 in the gas phase based on measurements in the absence of the La_2O_3 powder (Section 3.3).

According to Figures 9−12, the CH_4 conversion increases significantly in the presence of La_2O_3. The analysis of the species composition near the CH_4 side membrane interface and at the outlet allows us to conclude that reactions 15 and 16 occur on the surface of the La_2O_3 catalyst. C_2H_6 formed via reaction 16 is then converted to C_2H_4 and H_2 in the gas phase according to reaction 17. As discussed earlier, CO (and H_2) may form because of oxidation and/or reforming of CH_4, C_2H_6, and C_2H_4 as well as through the (reverse) WGS. At T = 750−850 °C, syngas production is low and kinetically frozen within the La_2O_3 catalyst but it is accelerated significantly at T = 900 °C. At this T, identifying the presence and rate of reactions producing syngas requires the use of computational models and is outside the scope of this work. A schematic of the global reaction pathways identified in our work is shown in Figure 16. With the exception of ODHE, these reactions are in agreement with the primary OCM reactions proposed by Stansch et al. who investigated the conventional OCM using a La_2O_3/CaO catalyst.[91]

Reactions 14−17 provide a macroscopic description of the OCM chemistry for BFZ91 and La_2O_3. Microscopically, several studies have already provided insight about the elementary steps

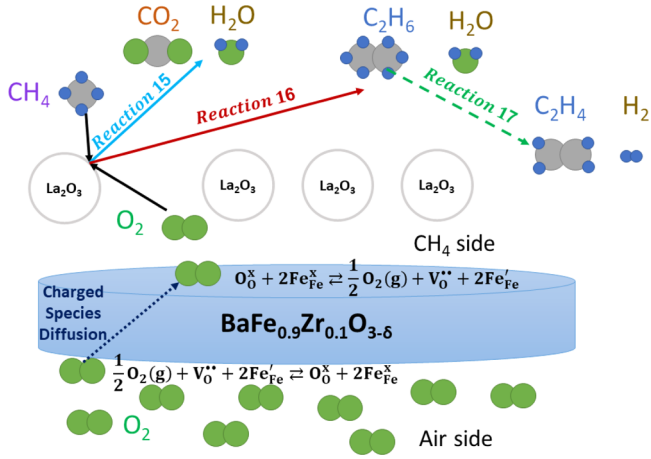

Figure 16. Schematic of the global reactions identified during OCM with BFZ91 membranes and La_2O_3 catalyst. Solid arrows correspond to reactions activated by the La_2O_3 catalyst. Dashed arrows represent gas-phase reactions. The dotted arrow signifies the transport of O_2 through the BFZ91 membrane. Reactions responsible for syngas production have been omitted.

of the OCM chemistry but significant disagreement still exists about the CH_4−O_2 activation process even for the same material. Early experiments have shown that CH_4 does not adsorb on the surface of La_2O_3.[89] This has been confirmed by computational studies suggesting that the CH_4 physisorption on La_2O_3 is very weak.[95] As a result, CH_4 is not expected to bind on La_2O_3 at any practical temperature. Instead, the CH_4 activation proceeds via a reaction that involves CH_4 in the gas-phase and an activated oxygen species (O_2^*) already adsorbed on La_2O_3 as follows:

$$O_2(g) + (s) \rightarrow O_2^*(s) \quad (18)$$

$$CH_4(g) + O_2^*(s) + (s) \rightarrow CH_3^\bullet(s) + HO_2^*(s) \quad (19)$$

$$CH_3^\bullet(s) \rightarrow CH_3^\bullet(g) + (s) \quad (20)$$

$$2CH_3^\bullet(g) \rightarrow C_2H_6(g) \quad (21)$$

In reactions 18−21, (s) denotes an empty site or a species on the surface of the catalyst. Reaction 18 corresponds to the gaseous O_2 adsorption on the surface of the catalyst and its activation to form O_2^*, while reaction 19 denotes the hydrogen abstraction from CH_4 in the presence of O_2^* leading to the formation of methyl radicals ($CH_3^\bullet$) on the surface of the catalyst. The process continues with $CH_3^\bullet$ desorption into the gas phase through reaction 20, whose existence has been confirmed experimentally.[56] Two $CH_3^\bullet$ will combine in the gas phase to form gaseous C_2H_6 through reaction 21. Then, C_2H_6 can in general be dehydrogenated to C_2H_4 through oxidative or non-oxidative pathways, as proposed in other studies.[26,90,96] Our results show that, within our membrane reactor, the NODHE in the gas phase (reaction 17) is the primary reaction for producing C_2H_4.

Reaction 19 is probably the most important step of the OCM chemistry as it is typically considered rate limiting toward C_2 formation. However, the exact mechanism is still under debate and depends strongly on the catalyst's properties. On the one side, it has been proposed that the C−H bond cleavage is homolytic and is activated by a surface O_2^* in a single step, as proposed by reaction 19.[26,90,97] In contrast, a heterolytic C−H

https://dx.doi.org/10.1021/acscatal.0c04888
ACS Catal. 2021, 11, 3638−3661

bond splitting on the surface of the catalyst has also been considered.[89,90,96] For La_2O_3, Wang et al. demonstrated computationally that reaction 19 proceeds on the (001) surface in two steps: the first step involves a heterolytic CH_3-H bond splitting with CH_3^- binding on a La^{3+} bridge site and H^+ binding on a neighboring O^{2-} site through an acid−base pair mechanism; after $CH_3^\bullet$ desorption into the gas phase, the second step involves the activation of another CH_4 on the La^{3+} bridge site forming $CH_3^\bullet$ through homolytic hydrogen abstraction from CH_4 induced by the activated O_2^* surface species.[95]

A second source of disagreement is related to the activated O_2^* species that favors the production of $CH_3^\bullet$ and hence C_2. In general, several oxygen species such as superoxide (O_2^{1-}), peroxide (O_2^{2-}), oxygen radical (O^{1-}), and O^{2-} may evolve on the surface of a catalyst. Out of these, O^{2-} has been correlated with CH_4 full oxidation while the remaining species have been linked with C_2 production.[60,61,78] Isotope-exchange experiments performed by Lacombe et al. demonstrated that the adsorption of molecular O_2 on La_2O_3 happens dissociatively;[89] they also hypothesized that the electrophilic site formed during the O_2 adsorption on La_2O_3 is either O^{1-} or O_2^{1-}.[89] Earlier electron paramagnetic resonance spectroscopy measurements performed by Wang and Lunsford had already shown evidence of O_2^{1-} on the surface of La_2O_3.[98] A computational study by Palmer et al. confirmed the dissociative adsorption of molecular O_2 on the (001) plane of La_2O_3;[99] however, further binding with an oxygen ion on the La_2O_3 surface resulted in the formation of O_2^{2-},[99] which did not agree with the results of Wang and Lunsford.[98] A recent computational study predicted O_2^{1-} as the activated oxygen species on La_2O_3 during the second step of reaction 19.[95] Note, however, that the aforementioned studies[89,95,98,99] dealt exclusively with the determination of the active site upon O_2 adsorption on La_2O_3 without correlating it with the OCM activity of the catalyst; the latter has been demonstrated for other OCM catalysts and a link between the C_2 yield and the concentration of the activated O_2 species was established.[100] Identifying and quantifying active species on the surface of OCM catalysts using in situ characterization techniques and correlating these with the C_2 yield is expected to advance the start-of-the-art on OCM.

Finally, based on Supporting Information Figure S9, we have shown that the non-oxidative dehydrogenation of C_2H_6, C_2H_4, and CH_4 does not take place on La_2O_3 between T = 750−900 °C. Given that CH_4 does not adsorb on La_2O_3,[89,95] it is reasonable to assume the same for C_2H_6 and C_2H_4. Fundamentally, this could explain the results shown in Supporting Information Figure S9. However, further studies based on isotope-exchange measurements are required to confirm this hypothesis.

4. CONCLUSIONS

This work investigates OCM in CMRs as a means to produce C_2 hydrocarbons from CH_4. A BFZ91 membrane was used for O_2 separation from air and La_2O_3 was selected as the OCM catalyst. Long-term experiments were conducted in a button-cell reactor at T = 750−900 °C and $X_{CH_4}^{in}$ = 0 − 30%. These measurements reveal that the BFZ91-La_2O_3 combination is chemically and structurally stable for 23 days, during which no loss of performance was observed. The performance of the materials was also investigated under partial O_2 consumption and pure CH_4 conditions. The BFZ91 membrane and La_2O_3 catalyst were characterized before and after the OCM measurements and significant information about each was obtained, especially regarding their stability under OCM conditions. The highest C_2 yield is ∼10% obtained at C_2 selectivity of ∼39%. These values were achieved at T = 850 °C and $X_{CH_4}^{in}$ = 5% during which $J_{O_2} \approx$ 0.91 (μmol/cm^2/s). Experimental measurements in the absence of La_2O_3 revealed that the membrane does not catalyze CH_4 pyrolysis or oxidation on its surface at high rates, and hence, undesired CH_4 conversion to species other than C_2 because of the membrane presence is avoided. Based on the results presented in our work, the primary OCM chemistry within our reactor is identified to consist of: (1) the CH_4 full oxidation to CO_2 and H_2O, (2) the CH_4 oxidative coupling to C_2H_6 and H_2O, (3) the C_2H_6 non-oxidative dehydrogenation to C_2H_4 and H_2, and (4) the oxidation/reforming of CH_4, C_2H_6, and C_2H_4 combined with the (reverse) WGS to produce syngas. The first two reactions happen on La_2O_3 and the third takes place exclusively in the gas phase. The reactions in the fourth category are slow and kinetically frozen at T = 750−850 °C but they accelerate at T = 900 °C and can happen both in the gas phase and on the La_2O_3 catalyst. Based on early and recent experimental-computational results, the mechanism of C−H bond breaking and the oxygen activation on La_2O_3 was presented in an effort to deepen our understanding on the OCM chemistry from a microscopic level.

■ ASSOCIATED CONTENT

Supporting Information

The Supporting Information is available free of charge at https://pubs.acs.org/doi/10.1021/acscatal.0c04888.

Experimental setup for OCM measurements; loading of the La_2O_3 powder on the BFZ91 membrane; system of equations to estimate the performance metrics and $X_{H_2O}^{mem}$; XRD of the BFZ91 raw ash and calcined BFZ91 powder; CH_4 conversion using BFZ91 in the absence of a catalyst; La_2O_3 sintering at high T; C_2H_6 and C_2H_4 non-oxidative dehydrogenation in the presence and absence of La_2O_3; and BFZ91-La_2O_3 performance and characterization under partial O_2 consumption and pure CH_4 conditions (PDF)

■ AUTHOR INFORMATION

Corresponding Authors

Georgios Dimitrakopoulos − *Department of Mechanical Engineering, Department of Materials Science & Engineering, and Department of Nuclear Science & Engineering, Massachusetts Institute of Technology, Cambridge, Massachusetts 02139, United States;* orcid.org/0000-0001-6636-0517; Email: gdim@mit.edu

Ahmed F. Ghoniem − *Department of Mechanical Engineering, Massachusetts Institute of Technology, Cambridge, Massachusetts 02139, United States*; Email: ghoniem@mit.edu

Authors

Bonjae Koo − *Department of Mechanical Engineering, Massachusetts Institute of Technology, Cambridge, Massachusetts 02139, United States*

Bilge Yildiz − *Department of Materials Science & Engineering and Department of Nuclear Science & Engineering, Massachusetts Institute of Technology, Cambridge,*

https://dx.doi.org/10.1021/acscatal.0c04888
ACS Catal. 2021, 11, 3638−3661

Massachusetts 02139, United States; orcid.org/0000-0002-2688-5666

Complete contact information is available at: https://pubs.acs.org/10.1021/acscatal.0c04888

Notes

The authors declare no competing financial interest.

■ ACKNOWLEDGMENTS

The authors would like to thank Royal Dutch Shell for supporting this research through the MIT Energy Initiative Seed Fund Program. This work made use of the Materials Research Science and Engineering Center (MRSEC) facilities at MIT's Materials Research Lab (MRL), supported by the National Science Foundation (NSF) award no. DMR-14-19807.

■ REFERENCES

(1) Garside, M. *Production Capacity of Ethylene Worldwide in 2018 and 2030*; Statista, 2020, November, 2019.
(2) Garside, M. *Production of Selected Chemicals and Plastics in the United States in 2019, by Type*; Statista, August, 2020.
(3) Gao, Y.; Neal, L.; Ding, D.; Wu, W.; Baroi, C.; Gaffney, A. M.; Li, F. Recent Advances in Intensified Ethylene Production-A Review. *ACS Catal.* **2019**, *9*, 8592−8621.
(4) *Global Ethylene Industry Outlook to 2023—Capacity and Capital Expenditure Forecasts with Details of All Active and Planned Plants*; GlobalData, April, 2019.
(5) Sims, M. *US October Ethylene Contracts Settle up 0.75 Cent/lb*; ICIS, October, 2019.
(6) Gärtner, C. A.; van Veen, A. C.; Lercher, J. A. Oxidative Dehydrogenation of Ethane: Common Principles and Mechanistic Aspects. *ChemCatChem* **2013**, *5*, 3196−3217.
(7) Nowlin, T. E. *Business and Technology of the Global Polyethylene Industry*; John Willey & Sons and Scrivener Publishing, 2014.
(8) *The Future of Petrochemicals: Growth Surrounded by Uncertainty*; Deloitte, 2019.
(9) Worrell, E.; Price, L.; Neelis, M.; Galitsky, C.; Nan, Z. *World Best Practice Energy Intensity Values for Selected Industrial Sectors*; Lawrence Berkeley National Laboratory, 62806, 2007.
(10) Sholl, D. S.; Lively, R. P. Seven Chemical Separations to Change the World. *Nature* **2016**, *532*, 435−437.
(11) Keller, G.; Bhasin, M. M. Synthesis of Ethylene via Oxidative Coupling of Methane I. Determination of Active Catalysts. *J. Catal.* **1982**, *73*, 9−19.
(12) Karakaya, C.; Kee, R. J. Progress in the Direct Catalytic Conversion of Methane to Fuels and Chemicals. *Prog. Energy Combust. Sci.* **2016**, *55*, 60−97.
(13) Farrell, B. L.; Igenegbai, V. O.; Linic, S. A Viewpoint on Direct Methane Conversion to Ethane and Ethylene Using Oxidative Coupling on Solid Catalysts. *ACS Catal.* **2016**, *6*, 4340−4346.
(14) Ghoniem, A. F.; Zhao, Z.; Dimitrakopoulos, G. Gas Oxy Combustion and Conversion Technologies for Low Carbon Energy: Fundamentals, Modeling and Reactors. *Proc. Combust. Inst.* **2019**, *37*, 33−56.
(15) Schmack, R.; Friedrich, A.; Kondratenko, E. V.; Polte, J.; Werwatz, A.; Kraehnert, R. A Meta-Analysis of Catalytic Literature Data Reveals Property-Performance Correlations for the OCM Reaction. *Nat. Commun.* **2019**, *10*, 441.
(16) *Gemini—Natural Gas to Ethylene*; Siluria Technologies. http://siluria.com/Products/Gemini_-_Natural_Gas_to_Ethylene.
(17) Reyes, S. C.; Iglesia, E.; Kelkar, C. P. Kinetic-Transport Models of Bimodal Reaction Sequences-I. Homogeneous and Heterogeneous Pathways in Oxidative Coupling of Methane. *Chem. Eng. Sci.* **1993**, *48*, 2643−2661.
(18) Lunsford, J. H. Catalytic Conversion of Methane to More Useful Chemicals and Fuels: a Challenge for the 21st Century. *Catal. Today* **2000**, *63*, 165−174.
(19) Spallina, V.; Velarde, I. C.; Jimenez, J. A. M.; Godini, H. R.; Gallucci, F.; van Sint Annaland, M. Techno-Economic Assessment of Different Routes for Olefins Production Through the Oxidative Coupling of Methane (OCM): Advances in Benchmark Technologies. *Energy Convers. Manage.* **2017**, *154*, 244−261.
(20) Powell, J. B. Natural Gas Utilization: Current Status and Opportunities. *Catal. Today* **2020**, *356*, 27−36.
(21) Cruellas, A.; Bakker, J. J.; van Sint Annaland, M.; Medrano, J. A.; Gallucci, F. Techno-Economic Analysis of Oxidative Coupling of Methane: Current State of the Art and Future Perspectives. *Energy Convers. Manage.* **2019**, *198*, 111789.
(22) Cruellas, A.; Heezius, J.; Spallina, V.; van Sint Annaland, M.; Medrano, J. A.; Gallucci, F. Oxidative Coupling of Methane in Membrane Reactors; A Techno-Economic Assessment. *Processes* **2020**, *8*, 274.
(23) Lu, Y.; Dixon, A. G.; Moser, W. R.; Ma, Y. H.; Balachandran, U. Oxygen-Permeable Dense Membrane Reactor for the Oxidative Coupling of Methane. *J. Membr. Sci.* **2000**, *170*, 27−34.
(24) Othman, N. H.; Wu, Z.; Li, K. A Micro-Structured $La_{0.6}Sr_{0.4}Co_{0.2}Fe_{0.8}O_{3-\delta}$ Hollow Fibre Membrane Reactor for Oxidative Coupling of Methane. *J. Membr. Sci.* **2014**, *468*, 31−41.
(25) Akin, F. T.; Lin, Y. S. Oxidative Coupling of Methane in Dense Ceramic Membrane Reactor with High Yields. *AIChE J.* **2002**, *48*, 2298−2306.
(26) Karakaya, C.; Zhu, H.; Zohour, B.; Senkan, S.; Kee, R. J. Detailed Reaction Mechanisms for the Oxidative Coupling of Methane over La_2O_3/CeO_2 Nanofiber Fabric Catalysts. *ChemCatChem* **2017**, *9*, 4538−4551.
(27) Wu, X.-Y.; Ghoniem, A. F. Mixed Ionic-Electronic Conducting (MIEC) Membranes for Thermochemical Reduction of CO_2: A Review. *Prog. Energy Combust. Sci.* **2019**, *74*, 1−30.
(28) Dimitrakopoulos, G.; Ghoniem, A. F. A Two-Step Surface Exchange Mechanism and Detailed Defect Transport to Model Oxygen Permeation Through the $La_{0.9}Ca_{0.1}FeO_{3-\delta}$ Mixed-Conductor. *J. Membr. Sci.* **2016**, *510*, 209−219.
(29) Dimitrakopoulos, G.; Ghoniem, A. F. Developing a Multistep Surface Reaction Mechanism to Model the Impact of H_2 and CO on the Performance and Defect Chemistry of $La_{0.9}Ca_{0.1}FeO_{3-\delta}$ Mixed-Conductors. *J. Membr. Sci.* **2017**, *529*, 114−132.
(30) Hunt, A.; Dimitrakopoulos, G.; Kirchen, P.; Ghoniem, A. F. Measuring the Oxygen Profile and Permeation Flux Across an Ion Transport $La_{0.9}Ca_{0.1}FeO_{3-\delta}$ Membrane and the Development and Validation of a Multistep Surface Exchange Model. *J. Membr. Sci.* **2015**, *468*, 62−72.
(31) Hunt, A.; Dimitrakopoulos, G.; Ghoniem, A. F. Surface Oxygen Vacancy and Oxygen Permeation Flux Limits of Perovskite Ion Transport Membranes. *J. Membr. Sci.* **2015**, *489*, 248−257.
(32) Lee, W.; Han, J. W.; Chen, Y.; Cai, Z.; Yildiz, B. Cation Size Mismatch and Charge Interactions Drive Dopant Segregation at the Surfaces of Manganite Perovskites. *J. Am. Chem. Soc.* **2013**, *135*, 7909−7925.
(33) Igenegbai, V. O.; Meyer, R. J.; Linic, S. In Search of Membrane-Catalyst Materials for Oxidative Coupling of Methane: Performance and Phase Stability Studies of Gadolinium-Doped Barium Cerate and the Impact of Zr Doping. *Appl. Catal., B* **2018**, *230*, 29−35.
(34) Deibert, W.; Ivanova, M. E.; Baumann, S.; Guillon, O.; Meulenberg, W. A. Ion-Conducting Ceramic Membrane Reactors for High-Temperature Applications. *J. Membr. Sci.* **2017**, *543*, 79−97.
(35) Sunarso, J.; Hashim, S. S.; Zhu, N.; Zhou, W. Perovskite Oxides Applications in High Temperature Oxygen Separation, Solid Oxide Fuel Cell and Membrane Reactor: A Review. *Prog. Energy Combust. Sci.* **2017**, *61*, 57−77.
(36) Igenegbai, V. O.; Almallahi, R.; Meyer, R. J.; Linic, S. Oxidative Coupling of Methane over Hybrid Membrane/Catalyst Active Centers: Chemical Requirements for Prolonged Lifetime. *ACS Energy Lett.* **2019**, *4*, 1465−1470.
(37) Garcia-Fayos, J.; Lobera, M. P.; Balaguer, M.; Serra, J. M. Catalyst Screening for Oxidative Coupling of Methane Integrated in Membrane Reactors. *Front. Mater.* **2018**, *5*, 31.

(38) Othman, N. H.; Wu, Z.; Li, K. An Oxygen Permeable Membrane Microreactor With an In-Situ Deposited $Bi_{1.5}Y_{0.3}Sm_{0.2}O_{3-\delta}$ Catalyst for Oxidative Coupling of Methane. *J. Membr. Sci.* **2015**, *488*, 182−193.
(39) Tan, X.; Pang, Z.; Gu, Z.; Liu, S. Catalytic Perovskite Hollow Fibre Membrane Reactors for Methane Oxidative Coupling. *J. Membr. Sci.* **2007**, *302*, 109−114.
(40) Zheng, Y.; Lin, Y. S. Oxidative Coupling of Methane on Improved Bismuth Oxide Membrane Reactors. *AIChE J.* **2001**, *47*, 436−444.
(41) Cao, Z.; Jiang, H.; Luo, H.; Baumann, S.; Meulenberg, W. A.; Voss, H.; Caro, J. Simultaneous Overcome of the Equilibrium Limitations in BSCF Oxygen-Permeable Membrane Reactors: Water Splitting and Methane Coupling. *Catal. Today* **2012**, *193*, 2−7.
(42) Bucher, E.; Egger, A.; Caraman, G. B.; Sitte, W. Stability of the SOFC Cathode Material $Ba_{0.5}Sr_{0.5}Co_{0.8}Fe_{0.2}O_{3-\delta}$ in CO_2-Containing Atmospheres. *J. Electrochem. Soc.* **2008**, *155*, B1218−B1224.
(43) Almar, L.; Störmer, H.; Meffert, M.; Szász, J.; Wankmüller, F.; Gerthsen, D.; Ivers-Tiffée, E. Improved Phase Stability and CO_2 Poisoning Robustness of Y-Doped $Ba_{0.5}Sr_{0.5}Co_{0.8}Fe_{0.2}O_{3-\delta}$ SOFC Cathodes at Intermediate Temperatures. *ACS Appl. Energy Mater.* **2018**, *1*, 1316−1327.
(44) Zhang, R.; Taskinen, P. Experimental Investigation of Liquidus and Phase Stability in the $BaO - SiO_2$ Binary System. *J. Alloys Compd.* **2016**, *657*, 770−776.
(45) Chi, Y.; Li, T.; Wang, B.; Wu, Z.; Li, K. Morphology, Performance and Stability of Multi-Bore Capillary $La_{0.6}Sr_{0.4}Co_{0.2}Fe_{0.8}O_{3-\delta}$ Oxygen Transport Membranes. *J. Membr. Sci.* **2017**, *529*, 224−233.
(46) Hardy, J. S.; Coyle, C. A.; Bonnett, J. F.; Templeton, J. W.; Canfield, N. L.; Edwards, D. J.; Mahserejian, S. M.; Ge, L.; Ingram, B. J.; Stevenson, J. W. Evaluation of Cation Migration in Lanthanum Strontium Cobalt Ferrite Solid Oxide Fuel Cell Cathodes via In-Operando X-Ray Diffraction. *J. Mater. Chem. A* **2018**, *6*, 1787−1801.
(47) Viitanen, M.; v. Welzenis, R. G.; Brongersma, H. H.; van Berkel, F. P. F. Silica Poisoning of Oxygen Membranes. *Solid State Ionics* **2002**, *150*, 223−228.
(48) Perz, M.; Bucher, E.; Gspan, C.; Waldhäusl, J.; Hofer, F.; Sitte, W. Long-Term Degradation of $La_{0.6}Sr_{0.4}Co_{0.2}Fe_{0.8}O_{3-\delta}$ IT-SOFC Cathodes due to Silicon Poisoning. *Solid State Ionics* **2016**, *288*, 22−27.
(49) Chen, K.; Jiang, S. P. Surface Segregation in Solid Oxide Cell Oxygen Electrodes: Phenomena, Mitigation Strategies and Electrochemical Properties. *Electrochem. Energy Rev.* **2020**, *3*, 730−765.
(50) Palermo, A.; Holgadovazquez, J.; Lee, A.; Tikhov, M.; Lambert, R. Critical Influence of the Amorphous Silica-to-Cristobalite Phase Transition on the Performance of $Mn/Na_2WO_4/SiO_2$ Catalysts for the Oxidative Coupling of Methane. *J. Catal.* **1998**, *177*, 259−266.
(51) Arndt, S.; Otremba, T.; Simon, U.; Yildiz, M.; Schubert, H.; Schomäcker, R. $Mn - Na_2WO_4/SiO_2$ as Catalyst for the Oxidative Coupling of Methane. What is Really Known? *Appl. Catal., A* **2012**, *425*−*426*, 53−61.
(52) Rojac, T.; Bencan, A.; Drazic, G.; Kosec, M.; Damjanovic, D. Piezoelectric Nonlinearity and Frequency Dispersion of the Direct Piezoelectric Response of $BiFeO_3$ Ceramics. *J. Appl. Phys.* **2012**, *112*, 064114.
(53) Lv, J.; Wu, J.; Wu, W. Enhanced Electrical Properties of Quenched $(1-x)Bi_{1-y}Sm_yFeO_3 - xBiScO_3$ Lead-Free Ceramics. *J. Phys. Chem. C* **2015**, *119*, 21105−21115.
(54) Lin, Y. S.; Zeng, Y. Catalytic Properties of Oxygen Semipermeable Perovskite-Type Ceramic Membrane Materials for Oxidative Coupling of Methane. *J. Catal.* **1996**, *164*, 220−231.
(55) Arndt, S.; Simon, U.; Heitz, S.; Berthold, A.; Beck, B.; Görke, O.; Epping, J.-D.; Otremba, T.; Aksu, Y.; Irran, E.; Laugel, G.; Driess, M.; Schubert, H.; Schomäcker, R. Li-Doped MgO From Different Preparative Routes for the Oxidative Coupling of Methane. *Top. Catal.* **2011**, *54*, 1266−1285.
(56) Luo, L.; Tang, X.; Wang, W.; Wang, Y.; Sun, S.; Qi, F.; Huang, W. Methyl Radicals in Oxidative Coupling of Methane Directly Confirmed by Synchrotron VUV Photoionization Mass Spectroscopy. *Sci. Rep.* **2013**, *3*, 1625.
(57) Schucker, R. C.; Dimitrakopoulos, G.; Derrickson, K.; Kopeć, K. K.; Alahmadi, F.; Johnson, J. R.; Shao, L.; Ghoniem, A. F. Oxidative Dehydrogenation of Ethane to Ethylene in an Oxygen-Ion-Transport-Membrane Reactor: A Proposed Design for Process Intensification. *Ind. Eng. Chem. Res.* **2019**, *58*, 7989−7997.
(58) Dimitrakopoulos, G.; Schucker, R. C.; Derrickson, K.; Johnson, J. R.; Kopeć, K. K.; Shao, L.; Alahmadi, F.; Ghoniem, A. F. Hydrogen and Ethylene Production Through Water-Splitting and Ethane Dehydrogenation Using $BaFe_{0.9}Zr_{0.1}O_{3-\delta}$ Mixed-Conductors. *ECS Trans.* **2017**, *80*, 181−190.
(59) Yildiz, M.; Simon, U.; Otremba, T.; Aksu, Y.; Kailasam, K.; Thomas, A.; Schomäcker, R.; Arndt, S. Support Material Variation for the $Mn_xO_y - Na_2WO_4/SiO_2$ Catalyst. *Catal. Today* **2014**, *228*, 5−14.
(60) Song, J.; Sun, Y.; Ba, R.; Huang, S.; Zhao, Y.; Zhang, J.; Sun, Y.; Zhu, Y. Monodisperse $Sr - La_2O_3$ Hybrid Nanofibers for Oxidative Coupling of Methane to Synthesize C_2 Hydrocarbons. *Nanoscale* **2015**, *7*, 2260−2264.
(61) Huang, P.; Zhao, Y.; Zhang, J.; Zhu, Y.; Sun, Y. Exploiting Shape Effects of La_2O_3 Nanocatalysts for Oxidative Coupling of Methane Reaction. *Nanoscale* **2013**, *5*, 10844−10848.
(62) Schucker, R. C.; J. Derrickson, K.; K. Ali, A.; J. Caton, N. The Effect of Strontium Content on the Activity and Selectivity of Sr-Doped La_2O_3 Catalysts in Oxidative Coupling of Methane. *Appl. Catal., A* **2020**, *607*, 117827.
(63) Babilo, P.; Haile, S. M. Enhanced Sintering of Yttrium-Doped Barium Zirconate by Addition of ZnO. *J. Am. Ceram. Soc.* **2005**, *88*, 2362−2368.
(64) Dimitrakopoulos, G.; Ghoniem, A. F.; Yildiz, B. In Situ Catalyst Exsolution on Perovskite Oxides for the Production of *CO* and Synthesis Gas in Ceramic Membrane Reactors. *Sustainable Energy Fuels* **2019**, *3*, 2347−2355.
(65) Watanabe, K.; Takauchi, D.; Yuasa, M.; Kida, T.; Shimanoe, K.; Teraoka, Y.; Yamazoe, N. Oxygen Permeation Properties of Co-Free Perovskite-Type Oxide Membranes Based on $BaFe_{1-y}Zr_yO_{3-\delta}$. *J. Electrochem. Soc.* **2009**, *156*, E81−E85.
(66) Kida, T.; Takauchi, D.; Watanabe, K.; Yuasa, M.; Shimanoe, K.; Teraoka, Y.; Yamazoe, N. Oxygen Permeation Properties of Partially A-Site Substituted $BaFeO_{3-\delta}$ Perovskites. *J. Electrochem. Soc.* **2009**, *156*, E187−E191.
(67) Park, C. Y.; Lee, T. H.; Dorris, S. E.; Balachandran, U. A Cobalt-Free Oxygen Transport Membrane, $BaFe_{0.9}Zr_{0.1}O_{3-\delta}$, and its Application for Producing Hydrogen. *Int. J. Hydrogen Energy* **2013**, *38*, 6450−6459.
(68) Wang, J.; Saccoccio, M.; Chen, D.; Gao, Y.; Chen, C.; Ciucci, F. The Effect of A-Site and B-Site Substitution on $BaFeO_{3-\delta}$: An Investigation as a Cathode Material for Intermediate-Temperature Solid Oxide Fuel Cells. *J. Power Sources* **2015**, *297*, 511−518.
(69) Geary, T. C.; Adler, S. B. Oxygen Nonstoichiometry and Defect Chemistry of the Mixed Conductor $La_{0.9}Ca_{0.1}FeO_{3-\delta}$ at Low Oxygen Partial Pressure. *Solid State Ionics* **2013**, *253*, 88−93.
(70) Kuhn, M.; Hashimoto, S.; Sato, K.; Yashiro, K.; Mizusaki, J. Oxygen Nonstoichiometry, Thermo-Chemical Stability and Lattice Expansion of $La_{0.6}Sr_{0.4}FeO_{3-\delta}$. *Solid State Ionics* **2011**, *195*, 7−15.
(71) Fleming, P.; Farrell, R. A.; Holmes, J. D.; Morris, M. A. The Rapid Formation of $La(OH)_3$ from La_2O_3 Powders on Exposure to Water Vapor. *J. Am. Ceram. Soc.* **2010**, *93*, 1187−1194.
(72) Neumann, A.; Walter, D. The Thermal Transformation From Lanthanum Hydroxide to Lanthanum Hydroxide Oxide. *Thermochim. Acta* **2006**, *445*, 200−204.
(73) Zhu, J.; Gui, Z.; Ding, Y. A Simple Route to Lanthanum Hydroxide Nanorods. *Mater. Lett.* **2008**, *62*, 2373−2376.
(74) Ozawa, M.; Onoe, R.; Kato, H. Formation and Decomposition of Some Rare Earth (RE = La, Ce, Pr) Hydroxides and Oxides by Homogeneous Precipitation. *J. Alloys Compd.* **2006**, *408*−*412*, 556−559.
(75) Kim, S. J.; Han, W. K.; Kang, S. G.; Han, M. S.; Cheong, Y. H. Formation of Lanthanum Hydroxide and Oxide via Precipitation. *Solid State Phenom.* **2008**, *135*, 23−26.

https://dx.doi.org/10.1021/acscatal.0c04888
ACS Catal. 2021, 11, 3638−3661

(76) Jeevanandam, P.; Koltypin, Y.; Palchik, O.; Gedanken, A. Synthesis of Morphologically Controlled Lanthanum Carbonate Particles Using Ultrasound Irradiation. *J. Mater. Chem.* **2001**, *11*, 869−873.
(77) Shirsat, A. N.; Ali, M.; Kaimal, K. N. G.; Bharadwaj, S. R.; Das, D. Thermochemistry of $La_2O_2CO_3$ Decomposition. *Thermochim. Acta* **2003**, *399*, 167−170.
(78) Hou, Y.-H.; Han, W.-C.; Xia, W.-S.; Wan, H.-L. Structure Sensitivity of $La_2O_2CO_3$ Catalysts in the Oxidative Coupling of Methane. *ACS Catal.* **2015**, *5*, 1663−1674.
(79) Chase, M. W. *NIST-JANAF Thermochemical Tables*, 4th ed; Part I, Al-Co, Journal of Physical and Chemical Reference Data, Monograph No. 9; American Institute of Physics and the American Chemical Society, 1998.
(80) Morss, L. R.; Edelstein, N. M.; Fuger, J. *The Chemistry of the Actinide and Transactinide Elements*, 4th ed; Springer; Volume *1−6*, 2010.
(81) Konings, R. J. M.; Beneš, O.; Kovács, A.; Manara, D.; Sedmidubský, D.; Gorokhov, L.; Iorish, V. S.; Yungman, V.; Shenyavskaya, E.; Osina, E. The Thermodynamic Properties of the f-Elements and their Compounds. Part 2. The Lanthanide and Actinide Oxides. *J. Phys. Chem. Ref. Data* **2014**, *43*, 013101.
(82) Liu, Z.; Ho Li, J. P.; Vovk, E.; Zhu, Y.; Li, S.; Wang, S.; van Bavel, A. P.; Yang, Y. Online Kinetics Study of Oxidative Coupling of Methane over La_2O_3 for Methane Activation: What Is Behind the Distinguished Light-off Temperatures. *ACS Catal.* **2018**, *8*, 11761−11772.
(83) Dimitrakopoulos, G.; Ghoniem, A. F. Role of Gas-Phase and Surface Chemistry in Methane Reforming Using a $La_{0.9}Ca_{0.1}FeO_{3-\delta}$ Oxygen Transport Membrane. *Proc. Combust. Inst.* **2017**, *36*, 4347−4354.
(84) Kirchen, P.; Apo, D. J.; Hunt, A.; Ghoniem, A. F. A Novel Ion Transport Membrane Reactor for Fundamental Investigations of Oxygen Permeation and Oxy-Combustion Under Reactive Flow Conditions. *Proc. Combust. Inst.* **2013**, *34*, 3463−3470.
(85) Song, J.; Qiu, Z.; Gao, J.; Tan, X.; Sunarso, J.; Wang, S.; Liu, S. CO_2 Erosion of $BaCo_{0.85}Bi_{0.05}Zr_{0.1}O_{3-\delta}$ Perovskite Membranes Under Oxygen Permeating Conditions. *Sep. Purif. Technol.* **2018**, *207*, 133−141.
(86) Balachandran, U.; Dorris, S. E.; Emerson, J. E.; Lee, T. H.; Lu, Y.; Park, C. Y.; Picciolo, J. J. *Hydrogen Production by Water Dissociation Using Ceramic Membranes - Annual Report for FY 2010. ANL-11/07*; Argonne National Labs, February 7, 2011.
(87) Prakash, B.; Chakraverty, S. Realization of Atomically Flat Steps and Terraces Like Surface of $SrTiO_3$ (001) Single Crystal by Hot Water Etching and High Temperature Annealing. *Solid State Commun.* **2015**, *213−214*, 28−30.
(88) Sánchez, F.; Ocal, C.; Fontcuberta, J. Tailored Surfaces of Perovskite Oxide Substrates for Conducted Growth of Thin Films. *Chem. Soc. Rev.* **2014**, *43*, 2272−2285.
(89) Lacombe, S.; Zanthoff, H.; Mirodatos, C. Oxidative Coupling of Methane over Lanthana Catalysts. *J. Catal.* **1995**, *155*, 106−116.
(90) Lunsford, J. H. The Catalytic Oxidative Coupling of Methane. *Angew. Chem., Int. Ed. Engl.* **1995**, *34*, 970−980.
(91) Stansch, Z.; Mleczko, L.; Baerns, M. Comprehensive Kinetics of Oxidative Coupling of Methane over the La_2O_3/CaO Catalyst. *Ind. Eng. Chem. Res.* **1997**, *36*, 2568−2579.
(92) Choudhary, V. R.; Uphade, B. S.; Mulla, S. A. R. Coupling of Endothermic Thermal Cracking with Exothermic Oxidative Dehydrogenation of Ethane to Ethylene Using a Diluted SrO/La_2O_3 Catalyst. *Angew. Chem., Int. Ed.* **1995**, *34*, 665−666.
(93) Hayek, N. S.; Khlief, G. J.; Horani, F.; Gazit, O. M. Effect of Reaction Conditions on the Oxidative Coupling of Methane over Doped $MnO_x - Na_2WO_4/SiO_2$ Catalyst. *J. Catal.* **2019**, *376*, 25−31.
(94) Werny, M. J.; Wang, Y.; Girgsdies, F.; Schlögl, R.; Trunschke, A. Fluctuating Storage of the Active Phase in a $Mn - Na_2WO_4/SiO_2$ Catalyst for the Oxidative Coupling of Methane. *Angew. Chem., Int. Ed.* **2020**, *59*, 14921−14926.
(95) Wang, S.; Li, S.; Dixon, D. A. Mechanism of Selective and Complete Oxidation in La_2O_3-Catalyzed Oxidative Coupling of Methane. *Catal. Sci. Technol.* **2020**, *10*, 2602−2614.
(96) Choudhary, V. R.; Rane, V. H. Oxidative Coupling of Methane over La_2O_3. Influence of Catalyst Preparation on Surface Properties and Steady and Oscillating Reaction Behaviour. *J. Chem. Soc., Faraday Trans.* **1994**, *90*, 3357−3365.
(97) Ito, T.; Wang, J.; Lin, C. H.; Lunsford, J. H. Oxidative Dimerization of Methane over a Lithium-Promoted Magnesium Oxide Catalyst. *J. Am. Chem. Soc.* **1985**, *107*, 5062−5068.
(98) Wang, J. X.; Lunsford, J. H. Evidence for the Thermal Generation of Superoxide Ions on Lanthanum Oxide (La_2O_3). *J. Phys. Chem.* **1986**, *90*, 3890−3891.
(99) Palmer, M. S.; Neurock, M.; Olken, M. M. Periodic Density Functional Theory Study of the Dissociative Adsorption of Molecular Oxygen over La_2O_3. *J. Phys. Chem. B* **2002**, *106*, 6543−6547.
(100) Xu, J.; Zhang, Y.; Xu, X.; Fang, X.; Xi, R.; Liu, Y.; Zheng, R.; Wang, X. Constructing $La_2B_2O_7$ (B = Ti, Zr, Ce) Compounds with Three Typical Crystalline Phases for the Oxidative Coupling of Methane: The Effect of Phase Structures, Superoxide Anions, and Alkalinity on the Reactivity. *ACS Catal.* **2019**, *9*, 4030−4045.

https://dx.doi.org/10.1021/acscatal.0c04888
ACS Catal. 2021, 11, 3638−3661